HAL open science

Geomechanical model of the Marmara Sea region - I. 3-D contemporary kinematics

Tobias Hergert, Oliver Heidbach, Anne Bécel, Mireille Laigle

To cite this version:

Tobias Hergert, Oliver Heidbach, Anne Bécel, Mireille Laigle. Geomechanical model of the Marmara Sea region - I. 3-D contemporary kinematics. Geophysical Journal International, 2011, 185, pp.1073-1089. 10.1111/j.1365-246X.2011.04991.x . insu-03606475

HAL Id: insu-03606475

https://insu.hal.science/insu-03606475v1

Submitted on 12 Mar 2022

HAL is a multi-disciplinary open access archive for the deposit and dissemination of scientific research documents, whether they are published or not. The documents may come from teaching and research institutions in France or abroad, or from public or private research centers.

L'archive ouverte pluridisciplinaire **HAL**, est destinée au dépôt et à la diffusion de documents scientifiques de niveau recherche, publiés ou non, émanant des établissements d'enseignement et de recherche français ou étrangers, des laboratoires publics ou privés.

Distributed under a Creative Commons Attribution 4.0 International License

Geophysical Journal International

Geophys. J. Int. (2011) **185,** 1073–1089 doi: 10.1111/j.1365-246X.2011.04991.x

Geomechanical model of the Marmara Sea region—I. 3-D contemporary kinematics

Tobias Hergert,[1,2,*] Oliver Heidbach,[3] Anne Bécel[2,4] and Mireille Laigle[2]

[1]*Geophysical Institute, Karlsruhe Institute of Technology (KIT), Hertzstr. 16, 76187 Karlsruhe, Germany. E-mail: tobias.hergert@gpi.uni-karlsruhe.de*
[2]*Department of Seismology, UMR 7154, Institut de Physique du Globe de Paris, Case 89, Tour 24-14, 4ème étage, 4 Place Jussieu, 75252 Paris Cedex 05, France*
[3]*GFZ German Research Centre for Geosciences, Section 2.6 Seismic Hazard and Stress Field, Telegrafenberg, 14773 Potsdam, Germany*
[4]*CSIC-Instituto de Ciencias de la Tierra 'Jaume Almera', Dep. Estructura y Dinamica de la Tierra, Calle Lluis Sole i Sabaris, Barcelona, Spain*

Accepted 2011 February 17. Received 2011 February 10; in original form 2010 February 12

SUMMARY

We investigate by means of a 3-D geomechanical model the relationship between structural elements and contemporary kinematics in the Marmara Sea region, northwest Turkey. The recently imaged fault system beneath the Marmara Sea is incorporated into the model as frictional surfaces with varying strike and dip. The Main Marmara Fault is implemented as through-going and is accompanied by mostly non-vertical second-order faults. Topography, basement-topography and the Moho become mechanically effective through changes in density and elastic parameters across these horizons. The model is subjected to gravity and kinematic boundary conditions. The ultimate goal of this study is to set up a 3-D model that is consistent with both, kinematic observations and stress data. The stress results are presented in a complementary paper. In this paper we present the modelled long-term 3-D kinematics in terms of fault slip rates, rotations, vertical motion and sense of fault slip. The model results agree with Global Positioning System velocities, geological fault slip rates, palaeomagnetic measurements and with the observed pattern of subsidence and uplift. Furthermore, our tectonically driven vertical velocities can be linked to landscape and basin evolution and to features of sedimentation. Our results indicate that the Main Marmara Fault can be interpreted as a through-going fault that slips almost purely in a strike-slip sense. Nevertheless, and not contradictory to the previous statement, there is significant dip-slip motion at some sections of the Main Marmara Fault. The agreement of the modelled 3-D kinematics with model-independent observations supports that the main structural details of the fault system are accounted for. Sensitivity analysis of model parameters reveals that changes in rock properties and the initial stress state have minor influence on the 3-D kinematics. We conclude that the 3-D structure of the fault system is the key control of the kinematics. The slip rate of the Main Marmara Fault from our model is lower than previous estimates and shows high variability along strike (12.8–17.8 mm a^{-1}). The latter indicates that stress accumulation is non-uniform along strike.

Key words: Numerical solutions; Plate motions; Geomechanics; Transform faults; Tectonics and landscape evolution.

1 INTRODUCTION

With the 1999 Izmit earthquake a west-migrating sequence of strong earthquakes along the North Anatolian Fault (NAF) reached the eastern Marmara Sea region (Stein *et al.* 1997; Lorenzo-Martin *et al.* 2006). This event initiated numerous new research activities in the Marmara Sea to reveal the subsurface structure and kinematics with the broader goal to assess the seismic hazard of that region. Two results of these structural and kinematic investigations are of key importance. (1) The structure of the NAF in the Marmara Sea differs significantly from that further east where the NAF is primarily a single vertical fault (Şengör *et al.* 2005). In the Marmara Sea region the NAF splits into three major branches and beneath the Sea a complex fault system and deep basins with up to 6-km-thick sediment infill have been imaged (Le Pichon *et al.* 2001, 2003; Armijo *et al.* 2002; Parke *et al.* 2002; Carton *et al.* 2007; Laigle *et al.* 2008; Bécel *et al.* 2009, 2010). (2) Fault slip rates derived from geomechanical models that are constrained by interseismic GPS velocities are considerably higher than those derived from

*Now at: Landesforschungszentrum für Geothermie, Institute for Applied Geosciences, Karlsruhe Institute of Technology (KIT), Kaiserstrasse 12, 76128 Karlsruhe, Germany.

© 2011 The Authors
Geophysical Journal International © 2011 RAS

GJI Geodynamics and tectonics
Downloaded from https://academic.oup.com/gji/article/185/3/1073/601038 by guest on 12 March 2022

geological and palaeoseismological investigations. The latter are in the range of 14–19 mm a^{-1} (Armijo *et al.* 1999; Meghraoui *et al.* 2004; Rockwell *et al.* 2006, 2009), whereas models that use Global Positioning System (GPS) data predict fault slip rates of 17–28 mm a^{-1} on the northern branch of the NAF (Meade *et al.* 2002; Le Pichon *et al.* 2003; Flerit *et al.* 2004; Reilinger *et al.* 2006).

The state-of-the art knowledge of the subsurface structure below the Marmara Sea has been integrated into a geomechanical model by Hergert & Heidbach (2010) to derive the long-term kinematics. This model quantifies the slip rate on the Main Marmara Fault (MMF) to between 12.8 and 17.8 mm a^{-1}, which is markedly lower than previous estimates and similar to geological slip rates. The lower slip rate can be referred to slip partitioning on second-order faults and to internal deformation in between the faults (Hergert & Heidbach 2010).

In this paper we present additional kinematic results of this model such as rotation rates, dip slip rates and the sense of fault slip and discuss further comparison with other model-independent observations. Furthermore, we investigate the sensitivity of the fault slip rates due to changes in fault friction and material properties and explore the reliability of our slip rates with regard to boundary conditions and possible post-seismic relaxation due to historical earthquakes. We further discuss the implications of the results regarding the interpretation of the fault system and seismic hazard. The overall goal of our study is to set up a model that fits consistently the 3-D kinematic and dynamic observations in the Marmara Sea region. In the complementary paper by Hergert & Heidbach (2011, herein referenced as Paper II) the dynamic results of this model are presented.

2 GEODYNAMIC AND TECTONIC SETTING

The NAF is a right-lateral strike-slip fault forming the boundary between the Anatolian Plate and the Eurasian Plate (Fig. 1a, Şengör *et al.* 2005). Along the NAF the Anatolian Plate escapes westwards due to the indentation of the Arabian Plate into Eurasia (McKenzie 1972). This westward motion of Anatolia is permitted and facilitated by the SSW-directed roll-back of the Hellenic subduction zone leading to approximately NS-oriented backarc extension in the broader Aegean (Heidbach & Drewes 2003; Flerit *et al.* 2004). As a result of this interaction of plates the Anatolian plate undergoes a counterclockwise rotation (McClusky *et al.* 2000; Reilinger *et al.* 2006). The relative motion between the Anatolian Plate and the Eurasian Plate along the NAF amounts to 24 ± 1 mm a^{-1} (McClusky *et al.* 2000).

In NW Anatolia the NAF splays into three major branches (Armijo *et al.* 1999, 2002, Fig. 1b). The northern branch, termed MMF, enters the Marmara Sea at the Izmit Bay (Alpar & Yaltırak 2002; Cormier *et al.* 2006) and passes through the Marmara Sea (Le Pichon *et al.* 2001, 2003). Further to the west it crosses the Gelibolu Peninsula as the Ganos Fault and enters the Aegean at the Gulf of Saros (Yaltırak & Alpar 2002a). The middle branch passes Iznik Lake, follows the southern shore of the Marmara Sea from Gemlik Bay to Kapıdağ Peninsula where it turns to SW (Yaltırak & Alpar 2002b; Kurtuluş & Canbay 2007). The southern branch forms the southern rim of the Bursa Graben and enters the Aegean south of Biga Peninsula.

Within the Marmara Sea the MMF exhibits three major bends (Fig. 1c): (1) the releasing bend at the western end of Izmit Bay (Tuzla Bend), (2) the bend SW of Istanbul (Istanbul Bend) and (3) the restraining bend at the western Tekirdağ Basin (Ganos Bend). The Prince's Islands Segment between the Tuzla and Istanbul Bends steeply dips to SW and follows the base of a major bathymetric scarp at the northern rim of the Çınarcık Basin (Carton *et al.* 2007). The Central Segment between Istanbul Bend and the Central Basin is rather straight and vertical. The Central Basin is bounded at its rims by secondary faults that dip towards the main branch (Laigle *et al.* 2008; Bécel *et al.* 2010).

The MMF and associated secondary faults bound three major basins in the Marmara Sea that reach depths of over 1200 m bsl. (1) The Çınarcık Basin in the east, (2) the Central Basin in the middle and (3) the Tekirdağ Basin in the west. The basins are separated by the Central High and the Western High, respectively. The Imralı Basin is associated with a north-dipping normal fault at its southern rim (Laigle *et al.* 2008). The basins are not only bathymetric depressions but are even more expressed in the basement topography since the sediment thickness has now been imaged to exceed 6 km in the Çınarcık and Central Basins (Carton *et al.* 2007; Laigle *et al.* 2008).

Several tectonic models were proposed for the Marmara Sea. Based on the fault geometries it was interpreted as a system of active pull-apart basins (Armijo *et al.* 2002), or formerly active ones (Rangin *et al.* 2004). In another view the MMF is a single through-going pure strike-slip fault based on the observation that focal mechanisms along the MMF show predominantly strike-slip faulting and that the fault trace comes close to a small circle around the Euler pole of a Marmara block (Le Pichon *et al.* 2003). Interpretation of more recent seismic profiles suggests that the basins are asymmetric half grabens (McHugh *et al.* 2006) and that tilting of huge basement blocks is involved (Laigle *et al.* 2008; Bécel *et al.* 2009). Accordingly, the whole fault system would appear as a large-scale negative flower structure (Aksu *et al.* 2000; Koral 2007; Laigle *et al.* 2008).

3 MODEL CONCEPT AND INPUT

The aim of this study is to quantify consistently the contemporary 3-D kinematics and dynamics of the Marmara Sea region by means of a 3-D geomechanical model. This involves the solution of the complete set of equations for the equilibrium of forces in three dimensions.

The workflow is divided into three major steps. (1) Model geometry and rock properties: we implement the 3-D fault system and integrate the major 3-D inhomogeneities of rock properties that change across the basement-topography and the Moho. (2) Setting initial and boundary conditions, applying loads and numerical solution: we define an initial stress state accounting for gravity and an appropriate ratio of horizontal to vertical stress. We apply gravity and the load on the seafloor arising from the hydrostatic pressure exerted by the water column. We apply kinematic boundary conditions at the sides of the model, which we derive from a separate model that fits the observed kinematics of NW Anatolia (so-called submodelling technique). Slip on frictional faults, deformation and stress throughout the volume evolve in response to the remotely acting forces associated with plate motion. The numerical solution is obtained by application of the finite-element method. (3) Model results analysis: the model results are compared with model-independent observations. Sensitivity of the model results due to model parameter uncertainties and assumptions is discussed.

Downloaded from https://academic.oup.com/gji/article/185/3/1073/601038 by guest on 12 March 2022

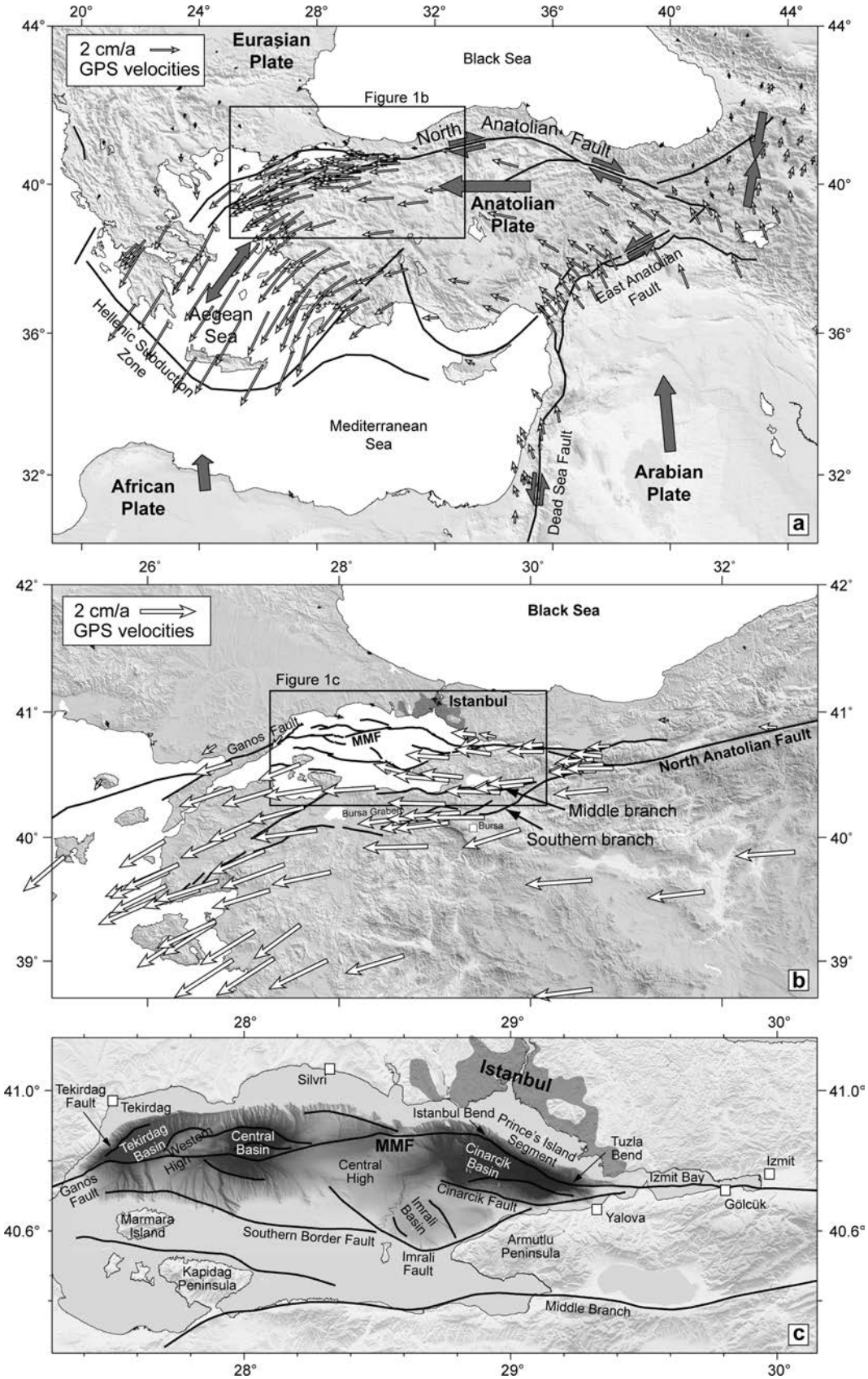

Figure 1. Geodynamic setting of the greater model area. (a) Tectonic map of the eastern Mediterranean. General plate motions (thick grey arrows) and GPS velocities (Reilinger *et al.* 2006; thin white arrows) with respect to Eurasia. Black lines mark faults. (b) Northwest Anatolia (area of the regional model; supplementary fig. 2 in Hergert & Heidbach 2010). GPS velocities from Reilinger *et al*. (2006) (thin white arrows) (c) Marmara Sea region (area of the Marmara model). Bathymetry from Le Pichon *et al*. (2001) and faults from Armijo *et al*. (2002) and Carton *et al*. (2007).

Downloaded from https://academic.oup.com/gji/article/185/3/1073/601038 by guest on 12 March 2022

3.1 Model geometry and rock properties

The geometry of our 3-D geomechanical model has a rectangular shape (27.25–30.25°E and 40.25–41.15°N) with 250 km EW and 100 km NS extent (Fig. 1c). The model is georeferenced in UTM (Universal Transverse Mercator) projection and its base is at 38 km bsl., which is below the Moho. The geometry comprises horizons that represent the Moho, the basement-topography and the topography/bathymetry. These layers are transsected by faults.

3.1.1 Moho

The Moho beneath the Marmara Sea and its surroundings is characterized by significant undulations of ∼10 km and a regional minimum depth right below the Sea. We generated a Moho map of northwest Anatolia using Moho depth data from various seismic experiments (Fig. S1, Supporting Information).

3.1.2 Topography, bathymetry and basement

Topography and bathymetry are incorporated into the model using the GTOPO30 digital elevation model (USGS) and the bathymetry of the North Marmara Trough (Le Pichon *et al.* 2001). Constraints on the basement structure beneath the Marmara Sea predominantly come from the SEISMARMARA Leg 1 seismic reflection–refraction experiment (Carton *et al.* 2007; Laigle *et al.* 2008; Bécel *et al.* 2009, 2010). A seismic velocity field was obtained by a 3-D tomographic inversion of the first arrival times of the SEISMARMARA Leg 1 shots recorded by an ocean bottom seismometer array (Bayrakcı 2009). The basement-topography below the Marmara Sea was basically taken as the 4.5 km s^{-1} *P*-wave isovelocity surface of a preliminary version of the 3-D velocity field. This velocity is typical for limestone that forms the pre-kinematic basement beneath the Marmara Sea (Parke *et al.* 2002). The velocity iso-surface was locally modified to ensure that it coincides with the basement-topography in depth-converted seismic sections and that it accounts for the stratigraphic constraints from wells (Ergün & Özel 1995; Elmas 2003). Vertical offsets in the basement-topography were established across those faults at which dip-slip is apparent in seismic profiles (Parke *et al.* 2002; Carton *et al.* 2007; Laigle *et al.* 2008). Outside the North Marmara Trough the basement-topography was constructed using the constraints from geological maps (Elmas & Yiğitbaş 2001) and reasonable assumptions, such as, that sediments are likely to be thick in topographic depressions or near releasing fault bends since these are favoured places of sediment deposition. The incorporated basement-topography is shown in Fig. 2(b).

3.1.3 3-D fault system

We constructed the fault geometry based on mapped fault traces at the seafloor, seismic sections and reasonable assumptions. We used the fault maps by Armijo *et al.* (2002), Cormier *et al.* (2006) and Carton *et al.* (2007) to constrain the upper termination of the faults. Information on the fault geometries in the subsurface comes from seismic profiles (Parke *et al.* 2002; Carton *et al.* 2007; Laigle *et al.* 2008; Bécel *et al.* 2009). These allow at least relative estimates of fault dips but absolute values of fault dips have also been suggested (Okay *et al.* 1999; Seeber *et al.* 2004; Kanbur *et al.* 2007; Bécel *et al.* 2010) or have been adopted to model the fault-related kinematics in the Marmara Sea (Muller & Aydin 2005). Generally, faults beneath the Marmara Sea dip rather steeply, also those, which are supposed to be normal faults.

In the case of uncertain fault geometry at depth we assumed that the fault trace at the surface is shifted to the west at depth due to the west migration of the Anatolian block relative to Eurasia. Thus, a change in fault strike is accompanied by a non-vertical dip of the fault. Furthermore, from an energetic point of view it is favourable for a fault to strike as straight as possible. Therefore, an apparent step-over or a small fault bend at the seafloor must not necessarily prolong at depth but likely adopts a more straight geometry. At least, this may be concluded from the rupture of the 1999 Izmit earthquake that revealed a straighter fault geometry in the Izmit Bay than presumed before (Alpar & Yaltırak 2002; Cormier *et al.* 2006). The dip direction of the implemented faults can be seen in Fig. 2(a).

We assume the MMF to penetrate the model in its whole depth (38 km bsl.). This may be an appropriate assumption for a plate boundary fault and it was proposed by Aksu *et al.* (2000) that the MMF extends to depths greater than 30 km. We further assume the MMF as being vertical below 15 km bsl. In the model the middle branch of the NAF reaches down to 20 km bsl., the Çınarcık Fault, Imralı Fault and Tekirdağ Fault to 15 km bsl., the Southern Border Fault to 10 km and the other faults to 7.5 km bsl.

In the Central Basin we assume the MMF as through-going, joining the southern inner rim of the basin in its uppermost part. Fig. 3 shows the final set of faults that are implemented into the model. The faults change gradually in dip and strike and are represented in the model by triangles whose size is ∼500 m. The changes in dip and strike are a key control for the kinematic and dynamic model results. The geometry of the model (3-D fault system, Moho and basement-topography) is provided in the Supporting Information.

3.1.4 Coefficient of friction

We implement the faults as frictional surfaces. Relative motion on these interfaces occurs when a critical shear stress is reached defined by the Mohr–Coulomb friction law.

$$\tau = C_0 + \mu(\sigma_n - P_f) = C_0 + \mu'\sigma_n. \quad (1)$$

Here, τ is shear stress, C_0 cohesion, μ the coefficient of friction, σ_n normal stress and P_f pore fluid pressure. σ_n is reduced by the magnitude of P_f, which facilitates fault slip. In the model an effective coefficient of friction μ' is assigned to the faults that implicitly accounts for P_f.

We assume C_0 to be negligible (Jamison & Cook 1980). Although the coefficient of friction μ of crustal rocks ranges between 0.6 and 0.85 (Byerlee 1978), observations at large-offset plate boundary faults indicate that these faults are weak and have low (effective) friction coefficients (Zoback *et al.* 1987; Reasenberg & Simpson 1992; Townend & Zoback 2004; d'Alessio *et al.* 2006), in agreement with a number of numerical models (e.g. Bird 1998; Jiménez-Munt & Sabadini 2002; Provost *et al.* 2003; Vernant & Chéry 2006). We test three different μ' distributions: (1) uniform $\mu' = 0.05$ on all faults, (2) $\mu' = 0.03$ on all faults and (3) $\mu' = 0.05$ on the MMF and $\mu' = 0.6$ on all other faults.

3.1.5 Rock properties

In this study, we apply linear elastic rheology. 'Long-term' elasticity explains the effective elastic-brittle behaviour of continental crust although it is not elastic at all depths, and its capability to preserve

Downloaded from https://academic.oup.com/gji/article/185/3/1073/601038 by guest on 12 March 2022

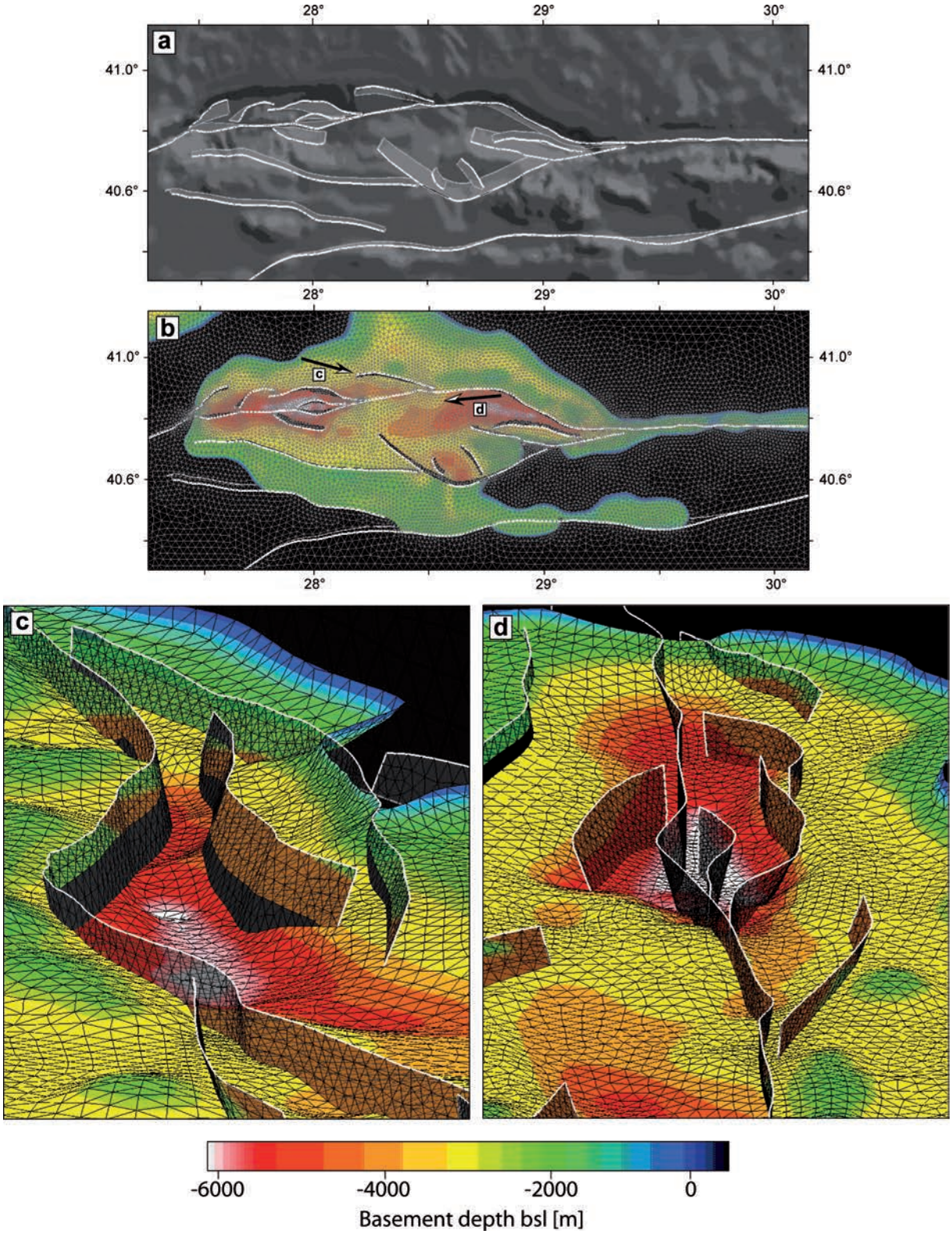

Figure 2. Fault system and basement-topography. (a) Topography and bathymetry. Fault traces at the surface (white lines) and at their lower ends (grey lines) indicate fault dips. (b) FE-mesh at the surface (grey), basement-topography where it is overlain by sediments (contours) and faults. Arrows show the view direction in Figs 3(c) and (d). (c) Çınarcık Basin. View from the northern shelf to ESE. Istanbul Bend (left), Izmit Bay (background, left), Central High (foreground, right), MMF (from background, left to foreground, right), inner (middle) and outer (right to background, left) Çınarcık Faults. White lines mark fault traces at the sea bottom. Visible parts of the faults are within the sediments. Note the vertical step in basement-topography across the basin bounding faults as revealed by Carton *et al.* (2007). (d) View from east to west. Central High (foreground), Central Basin (middle) and Tekirdağ Basin (background). The MMF was assumed as a through-going fault joining the southern inner rim of the Central Basin.

Downloaded from https://academic.oup.com/gji/article/185/3/1073/601038 by guest on 12 March 2022

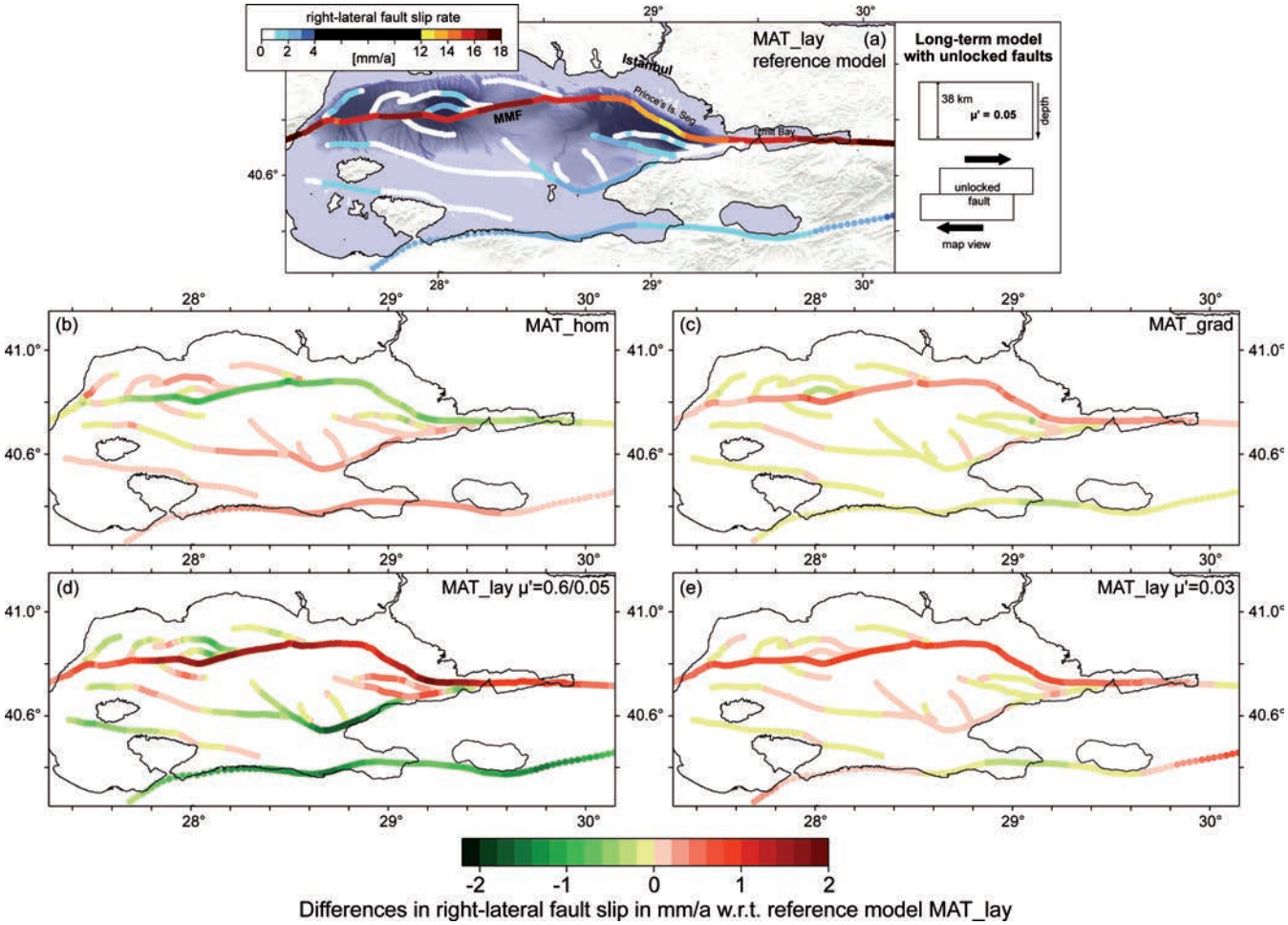

Figure 3. Influence of material properties and friction coefficient on fault slip rates. (a) Fault slip rates from the reference model ($\mu' = 0.05$ on all faults; MAT_lay, Table 1) (Hergert & Heidbach 2010). The sketch on the right-hand side shows that fault slip is driven by the far-field kinematics with the fault being unlocked. (b–e) Differences in right-lateral fault slip rate between the reference model and models with modified material properties or friction. (b) MAT_hom and $\mu' = 0.05$, (c) MAT_grad and $\mu' = 0.05$, (d) MAT_lay and $\mu' = 0.05$ on MMF and $\mu' = 0.6$ on other faults and (e) MAT_lay and $\mu' = 0.03$ on all faults.

Table 1. Elastic parameters and densities for three different rock property distributions.

Label	E (GPa)[a]	ν[a]	ρ (g cm^{-3})[a]
MAT_hom	70	0.25	2.65
MAT_lay	10/70/150	0.35/0.25/0.25	2.2/2.65/3.3
MAT_grad[b]	1–20/50–75-120/150	0.47–0.27/0.25/0.25	1.7–2.3/2.5–2.7–3.0/3.3

[a]In each column the first number refers to the sediments, the second to the basement and the third to the upper mantle.
[b]See Fig. S2.

strength over long periods (Armijo *et al.* 2003; Hubert-Ferrari *et al.* 2003).

For our model we consider three different distributions of density and elastic parameters (in terms of Young's modulus E and Poisson's ratio ν, Table 1). (1) Homogeneous rock properties throughout the model, thus ignoring the basement-topography and Moho (MAT_hom). (2) A layered distribution considering the sediments, basement and upper mantle, each characterized by uniform properties (MAT_lay). (3) A vertical gradient in rock properties within the sediments and basement (MAT_grad). Herein, values of rock properties are specified at the topography/bathymetry, basement-topography and Moho and are linearly interpolated in between vertically (Fig. S2, Supporting Information). Since these interfaces vary laterally with depth this represents a combination of local geometries and depth gradient.

The adopted values for the rock properties are based on constraints from seismic velocities. We used empirical relations (Brocher 2005) to convert P-wave velocities into S-wave velocities and rock densities and finally into elastic parameters. P-wave velocities in the basins of the North Marmara Trough are as low as 1.6 km s^{-1} in the uppermost kilometre and increase to 3.8 km s^{-1} below, while average velocities in the sediments are in the range of 2–2.5 km s^{-1}. The basement-topography was taken as the 4.5 km s^{-1} iso-surface (3.1.2). For the crystalline basement and for an ~10-km-thick lower crust, velocities of 5.7–6.3 km s^{-1} and 6.7 km s^{-1}, respectively, were inferred. The different rock property distributions are tested using uniform friction ($\mu' = 0.05$) on all faults.

3.2 Initial and boundary conditions, loads and numerical solution

3.2.1 Kinematic boundary conditions

To obtain kinematic boundary conditions consistent with the observed regional kinematics we use a larger scale model (termed

Downloaded from https://academic.oup.com/gji/article/185/3/1073/601038 by guest on 12 March 2022

regional model in the following, supplementary fig. 2 in Hergert & Heidbach 2010). This regional model is also 3-D and serves to generate a velocity field of Northwest Anatolia. This velocity field is used to drive the local Marmara model at its lateral boundaries by interpolating the nodal velocities of the regional model onto the boundary nodes of the Marmara model. Driving the model from its lateral sides rather than from below is appropriate as the forces that drive the plates in the Eastern Mediterranean are lateral forces due to the backarc extension in the Aegan and the indentation of the Arabian plate (Fig. 1).

For the lateral boundary conditions of the regional model we assume that on the crustal scale no vertical gradients in horizontal velocity exist at the boundaries of the regional model. This implies that mantle flow does not contribute to plate motion, neither by driving nor by retarding via viscous basal shear. Thus the bottom of our model is assumed to be shear stress free. Indication for such a strong crust–mantle coupling comes from the observed pattern of shear wave anisotropy. In the broader Aegean Hatzfeld *et al.* (2001) found the direction of fast polarization and the magnitude of delay times in good correlation with the present-day strain rate observed at the surface deduced from both, geodetic measurements and seismicity. Biryol *et al.* (2008) made the same observation at the NAF and concluded that the upper mantle and upper crust deform coherently.

We apply the rotation of the Anatolian and Marmara Plates around their respective Euler poles (Reilinger *et al.* 2006). At the southern model boundary between 29° and 32°E we replace rotation by uniform velocity that is defined by the rigid rotation velocity of the Anatolian Plate at 32°E at the model boundary. Between 29° and 28°E a linear transition leads over to the rigid rotation velocities west of 28°E (supplementary fig. 2 in Hergert & Heidbach 2010). This modification is necessary to avoid too southerly directed velocities at the southern boundary of the Marmara model. The northern boundary of the regional model is laterally fixed because vanishing velocities are observed there. Velocities at the eastern and western model boundaries north of the NAF are constrained to zero in E–W direction while motion is unconstrained parallel to the boundaries.

The 3-D velocity field generated by the regional model is used as boundary condition for the Marmara model at its boundaries south of the northern branch of the NAF. The boundary conditions north of the NAF are the same as those for the regional model, that is, laterally fixed northern boundary and zero E–W velocities at the western and eastern boundaries north of the NAF. At the bottom of the model vertical displacements are constrained to zero, whereas lateral motions are permitted. The surface is free of constraints.

3.2.2 Loads and initial stress state

Gravity is applied as a distributed volume load at an acceleration of 9.81 m s^{-2}. Surfaces below sea level are subjected to hydrostatic pressure due to the weight of the water column of the overlying sea. This is performed by applying a distributed surface load acting perpendicular to the local bathymetry at a pressure corresponding to the local water depth. Furthermore, the model is subjected to an initial stress state. As the kinematic results are not sensitive with regard to an initial stress state in equilibrium we do not describe it in this paper, but in Paper II where it is essential for the modelled stress state.

3.2.3 Numerical solution

The numerical problem is solved by applying the finite-element method (Zienkiewicz & Tayler 1994). The 3-D model volume is discretized into 640 000 linear tetrahedral elements allowing a resolution of a few hundred metres in the most critical areas and 2–3 km near the model boundaries. For the numerical solution we used the implicit solver of the commercial finite-element software Abaqus^{TM}. The model time is 20 ka.

3.3 Comparison of model results with observations

To validate the model we compare the results with model-independent observations such as GPS-derived velocities, fault-slip rates, palaeomagnetic measurements, information on vertical motion, geomorphology, information on stress and seismicity distribution. In this paper, Paper I, we present and discuss the kinematic model results and compare them with kinematic observations. The dynamic results are presented in the complementary Paper II.

4 FAULT SLIP RATES

We model the long-term kinematics by applying kinematic boundary conditions, while low-frictional faults slip continuously in response to the stresses they experience. The fault slip rates from this model have been presented by Hergert & Heidbach (2010). Their main result is that the MMF accommodates for most but not all of the relative plate motion, and that fault slip rates vary significantly along strike of the MMF with smaller slip rate on the Prince's Islands segment (minimum rate 12.8 mm a^{-1}) than in the Gulf of Izmit and on the Ganos Fault (maximum rate 17.8 mm a^{-1}). The other faults slip at rates in the range of 0–3.2 mm a^{-1}. Locking of faults at seismogenic depths (above 15 bsl.) confirms that the associated interseismic velocities agree with velocities derived from GPS observations (Hergert & Heidbach 2010).

In the following we discuss the sensitivity of the modelled fault slip rates beyond the analysis presented in the supplementary information of Hergert & Heidbach (2010) and we discuss how the modelled fault slip rates compare with other estimates of the fault slip rates.

4.1 Sensitivity of modelled fault slip rates

4.1.1 Post-seismic effects

Our assumption of elastic rheology implies that viscoelastic relaxation processes due to historical earthquakes do not affect the GPS velocities in the decade prior to the 1999 Izmit earthquake. The two major earthquakes in the Marmara region that could have caused significant post-seismic motion in the pre-1999 GPS data are the $M \sim 7.0$ 1894 and $M = 7.4$ 1912 earthquakes (Parsons 2004). We expand the model to non-linear, temperature-controlled visco-elastic rheology and incorporate the coseismic slip of these events into the model. The tests show that post-seismic effects are negligible (for details see Fig. S3, Supporting Information).

4.1.2 Boundary conditions and model dimension

To model fault slip rates using a model in which faults are unlocked, we apply lateral kinematic boundary conditions that represent long-term velocities. We use the same boundary conditions to drive the locked-fault model to produce interseismic velocities that can be compared with GPS observations (Hergert & Heidbach 2010). This assumption implies that strain associated with the seismic cycle is negligible at the boundaries of the model. Here we discuss whether

Downloaded from https://academic.oup.com/gji/article/185/3/1073/601038 by guest on 12 March 2022

actually interseismic velocities correspond to long-term velocities at the boundaries of the model and whether the applied boundary conditions are appropriate to derive fault slip rates.

Mayer & Lu (2001) inferred the pre-1999 strain profile across the NAF from InSAR observations of this earthquake. They found that the area affected by coseismic surface displacement was ∼55 km on either side of the fault and they estimated that 50 per cent of strain was stored within a distance of 10 km of the fault because of the rapid decay of strain with distance from the fault. Our model has a north–south width of 100 km with the main branch right in the middle so that the dimensions of the model are such that the interseismic strain essentially vanishes at the boundaries.

To check this in more detail we estimate the long-term velocity at GPS site SILE (Reilinger *et al.* 2006), which is located close to the northern boundary of the Marmara model. At this site the horizontal velocity during the decade prior to the 1999 Izmit earthquake was 0.85 ± 1.25 mm a^{-1} to the west (Reilinger *et al.* 2006). The coseismic displacement during the Izmit earthquake was 11.91 cm to the east (Reilinger *et al.* 2000). If we assume that the SILE site moves at the pre-Izmit velocity during the whole interseismic period of ∼280 yr (1719–1999), then we obtain a long-term velocity of 0.42 mm a^{-1} to the west. However, this is an upper bound for the long-term west velocity because post-seismic processes add an east-directed component. So our fixed northern model boundary over the long term is a fair assumption for our estimation of the fault slip rate.

At the southern model boundary interseismic deformation arising from the locked middle and southern branches of the NAF may be relevant so that long-term velocities near the southern model boundary may be little greater than those observed and applied. However, the slip rate on these faults is rather small. Hergert & Heidbach (2010) showed that a 10 per cent increase in velocities at the southern boundary of the regional model would increase resulting slip rates by 2 mm a^{-1}.

4.1.3 Material parameters and coefficient of friction

We also investigate the influence of the material properties and the coefficient of friction on the modelled slip rates beyond the tests presented in the supplementary information of Hergert & Heidbach (2010). At first we keep friction constant ($\mu' = 0.05$ on all faults) and vary density and elastic parameters. Fault slip rates on the MMF from the homogeneous model (MAT_hom, Table 1) are lower by maximum 1.0 mm a^{-1} compared to the rates from the model with layered rock properties (MAT_lay, Table 1), whereas slip rates on the other faults are slightly greater by <0.5 mm a^{-1} (Fig. 3b). The model with vertical gradients in rock properties (MAT_grad, Table 1) yields greater (<0.7 mm a^{-1}) slip rates on the MMF than the MAT_lay model (Fig. 3c). The greater MMF slip rates resulting from the inhomogeneous models compared to the homogeneous model can be referred to their greater Young's modulus in the lower crust and to their lower density of the sediments (Table 1, Fig. S2). The effect of greater Young's modulus, hence stiffer material, is that deformation becomes more localized at faults and that internal deformation is hampered. Besides, velocities at the model boundary are transmitted more effectively into the interior of the model volume. The effect of lower densities is reduced lithostatic stress at depth and hence lower fault normal stress, which at the same coefficient of friction results in greater slip rates. To summarize, the influence of changes in rock properties on fault slip rates is for the investigated cases at most 1.2 mm a^{-1} (Figs 3b and c).

In the following tests we keep the MAT_lay rock properties and vary fault friction. Assigning $\mu' = 0.6$ to all faults except the MMF ($\mu' = 0.05$) reduces slip rates on the smaller faults by up to 1.8 mm a^{-1}, whereas the slip rate on the MMF increases by the same amount (Fig. 3d). For $\mu' = 0.03$ on all faults the slip rate on the MMF increases by <1.0 mm a^{-1}, but slip rates on the other faults show only minor changes (Fig. 3e).

The coefficient of friction apparently rules the relative importance of localized fault slip and distributed deformation. In case of decoupled blocks at low μ' deformation is localized at faults. Distributed deformation in the volume gains importance as the degree of coupling increases with higher fault friction. In the model this relationship between off-fault deformation and fault slip is established as being dynamically consistent. The two alternative friction distributions in favour of increased slip rates on the MMF due to reduced slip partitioning (Fig. 3d) and reduced internal deformation (Fig. 3e) yield at most a 1.8 mm a^{-1} greater MMF slip rate.

The interseismic velocities from a model with altered elastic parameters fit the GPS observations similarly well (Hergert & Heidbach 2010). Also different friction coefficients on the secondary faults do not affect interseismic velocities because these faults terminate above the assumed locking depth of 15 km (Section 3.1.3).

4.2 Comparison with reported fault slip rates

Table 2 is a compilation of reported slip rates on the NAF, grouped by the different methods that were applied to derive these. Reported slip rates range between 2 and 31 mm a^{-1}. In general fault slip rates derived from geodetic observations exceed those from geological or palaeoseismological studies. In the following we discuss how our slip rates compare with the rates listed in Table 2.

Seismological fault slip rates use the released cumulative seismic moment in an area to derive the shear strain rate. In case of a complex fault system seismic fault slip rates likely denote the shear rate of the whole area rather than the slip rate on a single fault strand. In this case they represent an upper bound for the MMF. The reported rates of ∼20 mm a^{-1} in the Marmara Sea region (Table 2) agree with the modelled relative EW motion across the width of the model area.

Geological fault slip rates are inferred from the offset across a fault evolved during a certain period, either total offset since initiation of a fault or the offset of markers preserved in datable sedimentary strata. Reported geological fault slip rates are diverse which reflects different assumptions on total fault offset and uncertainties in dating (Table 2). The modelled slip rate on the MMF agrees well with reported estimates of 14–20 mm a^{-1} (Schindler 1997; Armijo *et al.* 1999).

Palaeoseismological investigations use coseismic displacements from historical earthquakes preserved in the subsurface to infer fault slip rates. The data listed in Table 2 refer mostly to the Ganos Fault located in the westernmost part of the model area. Here, our model predicts slip rates of ∼18 mm a^{-1}, which is in good agreement with the reported rates of 17–20 mm a^{-1}. At Gerede, which is located beyond the eastern model boundary, where the NAF is one single fault strand, the reported slip rate of 14–19 mm a^{-1} is similar to the modelled slip rate of 17.3 mm a^{-1} at the eastern model boundary. Palaeoseismological fault slip rates may represent a lower bound if coseismic slip at the surface is smaller than at depth.

Geological and palaeoseismological fault slip rates represent average relative plate motion over several seismic cycles, whereas geodetic fault slip rates rely on surface velocities within a fraction of a seismic cycle, when interseismic deformation due to locked

Downloaded from https://academic.oup.com/gji/article/185/3/1073/601038 by guest on 12 March 2022

Table 2. Compilation of right-lateral fault slip rates.

Slip rate (mm a^{-1})	Fault/Location	Reference
Seismological data		
31	NAF	Jackson & McKenzie (1984)
24	Marmara region	Eyidoğan (1988)
16	NAF western part	Kiratzi (1993)
16/12.1	Western NAF/Marmara Sea	Kiratzi & Papazachos (1995)
~ 20	Marmara region	Papazachos & Kiratzi (1996)
5.6	Marmara region @ 31°E	Pınar *et al*. (1996)
16–24/3	Marmara region/southern branch	Ambraseys (2002)
20 ± 4	Marmara region	Ambraseys (2006)
Geological data		
5–8	NAF	Barka & Kadinsky-Cade (1988)
2–4	Northern branch	Barka (1997)
14–20	Northern branch	Schindler (1997)
17	Marmara region	Armijo *et al*. (1999)
14	Northern branch	Armijo *et al*. (1999)
18 ± 3.5	Central NAF	Hubert-Ferrari *et al*. (2002)
10.5 ± 1.5	NAF in western Izmit Bay	Polonia *et al*. (2004)
20.5 ± 5.5	Central NAF (Eksik)	Kozacı *et al*. (2007)
18.6 ± 3.5	Central NAF (Tahtaköprü)	Kozacı *et al*. (2009)
Palaeoseismological data		
18	Ganos Fault (Saros Bay)	Rockwell *et al*. (2001)
≥ 17	Ganos Fault	Meghraoui *et al*. (2004)
18	Ganos Fault	Rockwell *et al*. (2006)
14–18/19	NAF (Gerede/1944 eq.)	Rockwell *et al*. (2006)
17.5–20	Ganos Fault	Aksoy *et al*. (2006)
6.3	Yenice-Gönen Fault	Kürçer *et al*. (2008)
GPS data directly		
25	NAF	Oral *et al*. (1995)
22.9	NAF	Noomen *et al*. (1996)
22 ± 3	Marmara region	Straub *et al*. (1997)
$\leq 24 \pm 1$	NAF	McClusky *et al*. (2000)
11/13/26	Izmit/Izmit Bay/Marmara Sea	Ayhan *et al*. (2002)
24–25	NAF	Reilinger *et al*. (2006)
GPS data in combination with rotation around a pole		
16/19	NAF @ 30°E / Marmara	Westaway (1994)
28	NAF	Le Pichon *et al*. (1995)
23	MMF, including Prince's Islands Segment	Le Pichon *et al*. (2003)
GPS data in combination with geomechanical modelling		
24/6	Northern/southern branch	Meade *et al*. (2002)
17	NAF	Provost *et al*. (2003)
17–20	Northern branch	Flerit *et al*. (2004)
18–24	Ganos Fault	Motagh *et al*. (2007)
3-D geomechanical model of this study		
12.8	Prince's Islands segment	Fig. 3(a)
15.8	Northern branch @ 29.5°E	Fig. 3(a)
17.8	Ganos Fault	Fig. 3(a)
3.2	Middle branch @ 29.5°E	Fig. 3(a)

faults is effective. A first-order approach to derive fault slip rates from geodetic observations is to use the difference in fault-parallel interseismic GPS velocities observed at either side of the fault and at some distance to the fault where the interseismic effect is small. This implies rigid-block rheology (which makes it a lower-bound estimate because interseismic deformation pretends a smaller relative motion) and refers the difference in velocity between the GPS sites exclusively to slip on the considered fault in between (which makes it an upper-bound estimate). In a similar way, rigid blocks have been defined that rotate at a rate and around a pole such that interseismic GPS velocities distributed over a larger area are optimally fitted (Le Pichon *et al.* 2003; Westaway 1994). Another approach to derive fault slip rates from interseismic GPS data is to use geomechanical models in which faults are embedded in deformable half-space and which relate the fault slip below a given locking depth to the surface velocities that fit the interseismic GPS data best. The derived fault slip rates depend in particular on the details of the fault geometries.

There are three studies providing slip rates for particular fault segments in the Marmara Sea region from GPS-constrained geomechanical models (Meade *et al.* 2002; Flerit *et al.* 2004; Reilinger *et al.* 2006). Fig. S4 (Supporting Information) shows the adopted fault geometries and the pertaining slip rates, which are 24.4–24.8 mm a^{-1} (Meade *et al.* 2002), 24.6–27.9 mm a^{-1} (Reilinger *et al.* 2006) and 17–20 mm a^{-1} (Flerit *et al.* 2004) on the MMF. Our slip rates (Fig. 3a) are significantly smaller and show high variability along fault strike. The slip rate on the MMF has been regarded as being uniform on its whole length, including the northern Çınarcık margin (Le Pichon *et al.* 2003), whereas our results show 5 mm a^{-1} variability of slip rate along the MMF (Fig. 3a).

The apparent conflict between geodetical and geological/palaeoseismological fault slip rates is commonly explained by evoking temporal changes in fault slip rates as the different methods capture time periods of different length (10^0–10^1a versus 10^2–10^6a). However, our results show that geodetic and geological/palaeoseismological fault slip rates can well be reconciled in the Marmara region because our fault slip rates agree with geological/palaeoseismological slip rates (Table 2) and fit the geodetic observations (Hergert & Heidbach 2010).

4.3 Origin of deviations in right-lateral fault slip rates

Even though the previous models and ours are constrained by essentially the same GPS observations and though all models fit the observations equally well, the resulting fault slip rates differ considerably from each other. This shows that fitting interseismic GPS velocities depends much on the adopted fault geometries and on whether internal deformation and a dynamically consistent evolution of fault slip is permitted. Hergert & Heidbach (2010) showed that the smaller fault slip rates predicted by this model can be attributed to (1) slip partitioning, that is, second-order faults contribute to relative plate motion thereby lowering the slip rate on the MMF (2) internal deformation, that is, deformation in the volume between faults, which may be comprised of rotations, permanent strain and slip on smaller faults not considered in the model and (3) dip-slip on non-vertical faults that strike oblique to the overall E–W direction of plate motion in the Marmara Sea region. Note, that part of relative plate motion is accommodated also beyond the southern boundary of the model, probably most of it on the southern branch of the NAF.

Slip partitioning has also been observed in other strike-slip fault systems such as the San Andreas Fault in California where it is paralleled by the Hayward, Calaveras, San Jacinto and other faults (Bilham & Bodin 1992; Geist & Andrews 2000), the Alpine Fault in New Zealand where it splits into the Marlborough Fault system (Norris & Cooper 2000) and the Dead Sea Fault that splits into the Yammouneh and Serghaya Faults (Gomez *et al.* 2007). The mechanism of slip partitioning is also effective through oblique and dip-slip motion on non-vertical faults. As a consequence of slip

Downloaded from https://academic.oup.com/gji/article/185/3/1073/601038 by guest on 12 March 2022

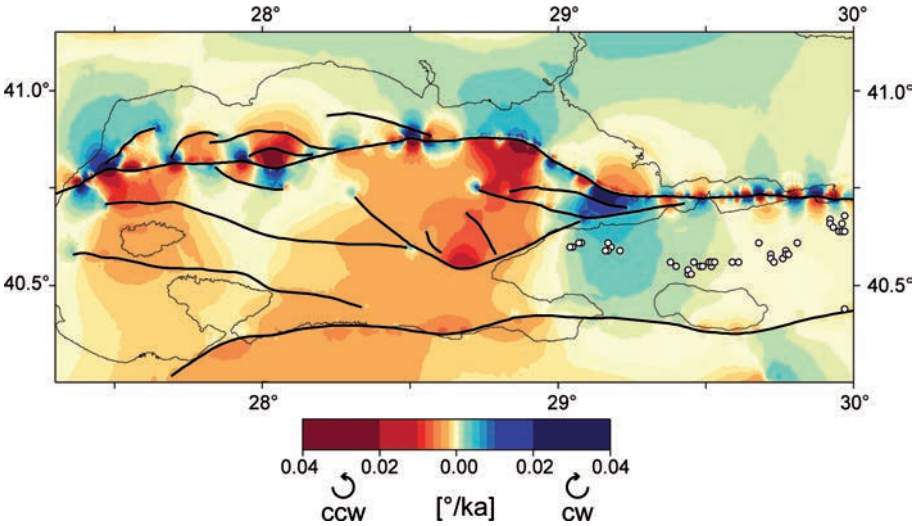

Figure 4. Rotation rates calculated from the modelled velocity field at the surface. Blue colours indicate clockwise rotation, red colours counter-clockwise rotations. White circles mark locations of the data by Avşar & İşseven (2009).

partitioning between strike-slip motion on a vertical fault and dip-slip motion on neighbouring non-vertical faults Jones & Wesnousky (1992) found a reduction of slip rate on the vertical San Andreas Fault by 50 per cent at some places compared to the case in which the dip-slip faults are not accounted for. Though faults below the Marmara Sea are steep this mechanism also contributes to lower slip rates on the MMF.

5 ROTATION RATES

Rotations may form some part of what we termed internal deformation. We calculated rotation rates from the modelled horizontal velocity field at the surface as the antisymmetric part of the velocity gradient field (e.g. Cai & Grafarend 2007)

$$\frac{1}{2}\left(\frac{\mathrm{d}V_{\mathrm{E}}}{\mathrm{d}N} - \frac{\mathrm{d}V_{\mathrm{N}}}{\mathrm{d}E}\right), \tag{2}$$

where V_{E} and V_{N} are the velocities in east and north directions, respectively. The eastern Çınarcık Basin, Armutlu Peninsula and the area north of the NAF are found to rotate clockwise, whereas the Tekirdağ Basin, Central Basin, Imralı Basin and Western Çınarcık Basin as well as the southern part of the Marmara Sea show counter-clockwise rotations (Fig. 4). The highest rotation rates are associated with fault bends.

There are several observations that support the modelled rotation rates. Modelled clockwise rotations east and west of the Bosphorus are confirmed by left-lateral faults emerged in a dextral shearing setting (Oktay *et al.* 2002). Counter-clockwise rotation characterizes most of the Marmara Sea area south of the MMF and in particular the basins, which agrees with the interpretation by Aksu *et al.* (2000). Clockwise rotation in the eastern Çınarcık Basin was quantified by Seeber *et al.* (2006) to occur at a rate of 0.018° ka^{-1} based on geometrical considerations, which is similar to the modelled rotation rates (Fig. 4). Clockwise rotation of Armutlu Peninsula has been reported based on GPS observations (Straub *et al.* 1997), palaeomagnetic measurements (Schindler 1997; Avşar & İşseven 2009) and structural fault characteristics indicating dextral shear (Alpar & Yaltırak 2002). Avşar & İşseven (2009) and references therein inferred clockwise rotation of Armutlu Peninsula at a rate of $16 \pm 6.8^{\circ}$ since Eocene times (38 Ma), that is, $4.2 \times 10^{-4}\,^{\circ}$ ka^{-1}. The model predicts somewhat higher rotation rates of between $5 \times 10^{-3}\,^{\circ}$ ka^{-1} to below $1 \times 10^{-3}\,^{\circ}$ ka^{-1} at the locations where the rock samples analysed by Avşar & İşseven (2009) originate (Fig. 4). Avşar & İşseven (2009) define rotation relative to Eurasia and mention the possibility that rotation may have commenced only with initiation of the NAF which is said to be 5 Ma (Armijo *et al.* 1999). In this case the rotation rate would be $3.2 \times 10^{-3}\,^{\circ}$ ka^{-1}, which is in the same order as our result.

6 VERTICAL VELOCTIES

As we solve the complete 3-D equations of equilibrium of forces our model also provides the vertical velocity field. Fig. 5 shows the modelled vertical velocity at the surface.

6.1 Subsiding basins

The highest subsidence rates in the Marmara Sea region appear in the North Marmara Trough (Fig. 5). Comparison of the modelled vertical motion pattern in the Marmara Sea with the bathymetry reveals that the areas of high subsidence rates coincide with the location and extent of the deep basins, namely the Tekirdağ Basin in the west (up to 3.6 mm a^{-1}), the Central Basin in the middle (up to 2.9 mm a^{-1}), the Çınarcık Basin in the east (up to 4.5 mm a^{-1}) and the Imralı Basin in the south (up to 1.4 mm a^{-1}) (Fig. 5).

The modelled rates are similar to vertical velocities inferred from submarine observations (Fig. 5, Table 3). Within the basins the highest modelled subsidence rates occur at the narrow ends of the Çınarcık and Tekirdağ Basins, which were found to form the depocentres of these basins (Seeber *et al.* 2004, 2006). The depocentres of these basins are visible in seismic profiles, in which fanning of sediments in the basins towards the depocentres is observed (Seeber *et al.* 2004, 2006; Carton *et al.* 2007; Laigle *et al.* 2008).

This model addresses the vertical velocities originating from plate tectonics but there are other active mechanisms affecting the morphology, for example, creeping slopes, sedimentation, compaction of soft soils or submarine landslides along the northern scarp of the North Marmara Trough. Thick sediment infill in the Imralı Basin explains why this basin is hardly expressed in the bathymetry but

Downloaded from https://academic.oup.com/gji/article/185/3/1073/601038 by guest on 12 March 2022

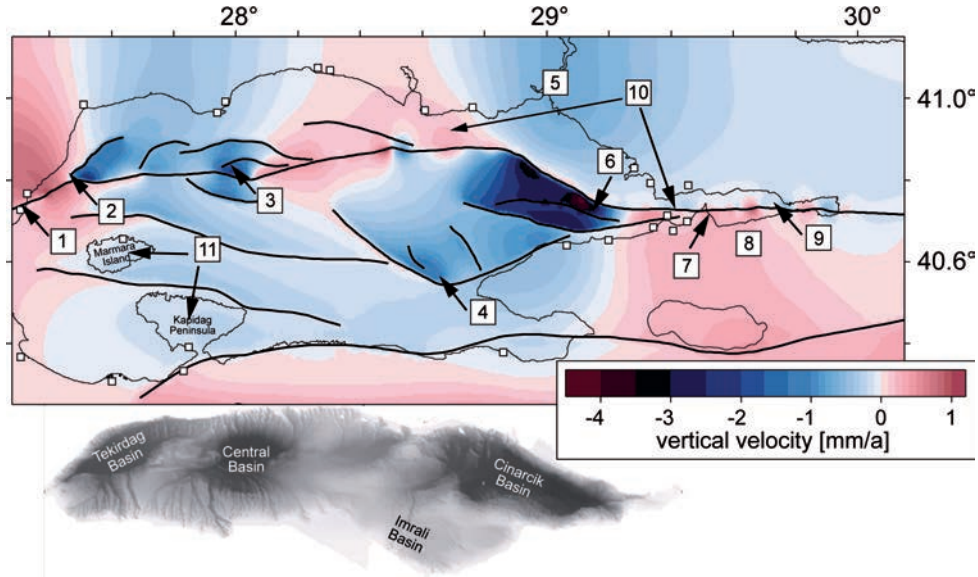

Figure 5. Modelled vertical velocity at the surface. Blue colours indicate subsidence, red colours uplift. Large squares with numbers refer to Table 3 in which observed vertical rates are summarized. Small squares mark uplifted marine terraces (Yaltırak *et al.* 2002).

Table 3. Reported information on vertical velocities.

Label (Fig. 5)	Vertical velocity (mm a^{-1})	Sense	Remarks	Reference
1	+0.3	Uplift	Marine terraces	Yaltırak *et al*. (2002)
2	−2.8	Subsidence	Sedimentation structure	Seeber *et al*. (2004)
3	−2 to −6	Subsidence	Max. throw rate at faults	Armijo *et al*. (2005)
4	−1 (−2)	Subsidence	Footwall collapse	McHugh *et al*. (2006)
5	−10 to +3		Persistent Scatterer InSAR	Walter *et al*. (2010)
6	−7.7 ± 1.3	Subsidence	Sedimentation structure	Seeber *et al.* (2006)
7	+0.3 to +0.4	Uplift	Marine terraces 12–15 m in 36 ka	Emre *et al*. (2006)
8	+0.224	Uplift	Armutlu block	Yaltırak & Alpar (2002a)
9	−8 (locally)	Subsidence	Sedimentation structure	Cormier *et al*. (2006)
10	−0.3 to −0.7		Relative subsidence (3–8 m in 12 ka) of Izmit Bay relative to the northern shelf	Cormier *et al*. (2006)
11			Southward tilt of islands	Parke *et al*. (2002)

actually the basement is downthrown by several kilometres (Laigle *et al.* 2008).

6.2 Fault-related vertical velocities

The highest modelled gradients in vertical motion occur at the faults along the rims of the basins (Fig. 5). This indicates that the modelled subsidence in the basins is fault related. The modelled dip-slip rates correlate with implemented fault dips (Figs 2a and 6). Less steep fault segments, such as the Prince's Islands Segment, the MMF at the Tekirdağ Basin and the Imralı Fault show the highest dip-slip rates. Furthermore, dip-slip rates depend on the orientation of the fault with respect to the EW-oriented plate motion and on the acting direction of extension (∼NE–SW). As a consequence, the releasing sides of bends and NW–SE striking faults show higher dip-slip rates (Fig. 6). Eventually, dip-slip rates depend on the lateral slip rate on a fault so that dip-slip rates on the MMF exceed those on the smaller faults.

6.3 Stable footwalls and tilting blocks

The footwalls of faults are quite stable with only minor subsidence rates or slight uplift such as along the Prince's Islands segment, the western part of the Imralı Fault, the Tekirdağ Fault and the MMF south of the Tekirdağ Basin (Fig. 5). This agrees with the findings of Seeber *et al.* (2004, 2006) and is generally characteristic for large normal faults in areas under extension (Okay & Okay 2002). Okay & Okay (2002) report footwall uplift at the MMF relative to the present sea level at a rate corresponding to 13 per cent of the hangingwall's subsidence in the Tekirdağ Basin. This is similar to the model results, which show footwall uplift adjacent to the Tekirdağ and Çınarcık Basins at 5–10 per cent of the rate at which the hangingwalls subside.

A basement block that is bounded by faults exhibiting dip-slip will tilt if the block represents the stable footwall on one side and the subsiding hangingwall on the other side. The modelled vertical velocities and dip-slip rates (Figs 5 and 6) explain the southward tilt of the blocks on top of which Marmara Island and Kapıdağ Peninsula are located and also the south- and northward dip of the basement below the Imralı and Çınarcık Basins, respectively. The dip of the basement below these basins is due to dip-slip at the Imralı Fault in contrast to the relatively stable footwall at the southern rim of the Çınarcık Basin and due to different rates in dip-slip at the faults bounding the Çınarcık Basin. The tilt of basement blocks is confirmed by dipping sedimentary layers revealed in seismic profiles (Carton *et al.* 2007; Laigle *et al.* 2008).

Downloaded from https://academic.oup.com/gji/article/185/3/1073/601038 by guest on 12 March 2022

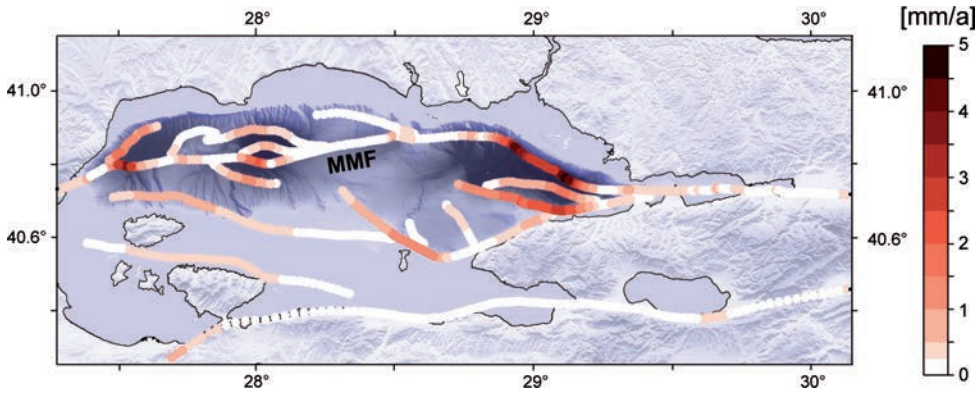

Figure 6. Dip-slip rates on faults at the surface. Footwalls and hangingwalls become clear from Fig. 5 (basically at faults north of the MMF the southern block subsides relative to the northern one and at faults south of the MMF vice versa).

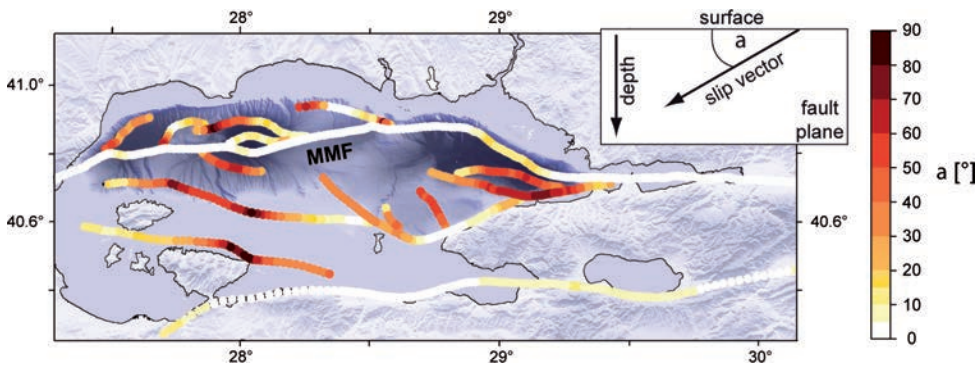

Figure 7. Absolute angle between a horizontal tangent at the fault and the 3-D slip-vector on the fault at the surface. Light colours correspond to strike-slip motion and dark colours to dip-slip motion.

6.4 Areas of uplift

In comparison with the vertical velocities shown by Hergert & Heidbach (2010), there is no longer subsidence along the southern and western shore of the Marmara Sea, but uplift despite the extensional boundary conditions (Fig. 5). The reason is that herein the 3-D (i.e. not only the horizontal but also the vertical) velocity field produced by the regional model drives the Marmara model south of the NAF. Probably, the southwest turn of the middle and southern branches of the NAF cause the uplift in the Strait of Çanakkale area. In this way, the applied submodelling technique takes mechanisms from outside the model area into account that affect the model's interior.

A maximum uplift rate near the western shore of the Marmara Sea reaches 1.2 mm a^{-1}. South of Izmit Bay between the northern and middle branches of the NAF and further to the south uplift is predicted at rates of 0.1–0.4 mm a^{-1}. The northern shelf and coastal area to the north of the Central Segment of the MMF shows little uplift of 0–0.2 mm a^{-1} and is basically stable.

The uplift to the west of the Marmara Sea has been attributed to the restraining Ganos Bend of the northern branch of the NAF (Seeber *et al.* 2004). Armutlu Peninsula and Samanlıda Massif have been interpreted to form a pressure ridge between the northern and middle branches of the NAF (Emre *et al.* 1998). Late Pleistocene marine terraces have been documented at several places above the present sea level around the Marmara Sea indicating uplift (Fig. 5). Modelled uplift mostly correlates, both in location and rate, with the location and uplift rates of these terraces, in particular along the western shore of the Marmara Sea and along the southern shore of the Izmit Bay (Fig. 5).

7 KINEMATICS AND FAULT GEOMETRY

From the presented results it becomes clear that fault geometries strongly affect the modelled kinematics. Here we show how the fault geometry in the Marmara Sea and the 3-D velocity field are related to each other.

Generally, the fault segments striking E–W to ENE–WSW slip at greater rates than those oriented oblique to this orientation (Fig. 3a). Further, modelled slip rates depend on the length and depth extent (see Section 3.1.3) of a fault. If the lower ends of the smaller faults were at greater depth than assumed, the slip rate on the MMF would decrease, whereas rates on the secondary faults would increase. Conversely, if the smaller faults would cease at shallower depths than assumed, some fraction of the cumulative slip rate on these faults would be additionally taken up by the MMF. However, this would not explain markedly higher slip rates on the MMF because the model with Byerlee coefficients of friction on the secondary faults represents the extreme case with negligible slip on the secondary faults (Fig. 3d). If the secondary faults and the MMF would connect with each other instead of being separated as assumed in the model for technical reasons then the effect of slip partitioning would be greater.

7.1 Sense of fault slip

To infer the sense of motion on the faults we calculate the absolute angle between a horizontal tangent at the local fault plane and the 3-D slip-vector on the fault (Fig. 7). We choose this representation rather than the rake because it is visually recognizable more easily.

Downloaded from https://academic.oup.com/gji/article/185/3/1073/601038 by guest on 12 March 2022

The MMF and the middle branch of the NAF are characterized by predominant strike-slip motion, whereas on the second-order faults oblique-slip or dip-slip motion prevails. Even along the Prince's Islands Segment this angle is small in the range of between 5° and at most 19° at the surface, which is basically strike-slip motion. At 15 km depth the sense of slip is even closer to pure strike-slip motion (maximum 9°) because dip-slip rate decreases (maximum dip-slip of 2.1 mm a^{-1} at 15 km depth in contrast to maximum 4.5 mm a^{-1} at the seafloor because MMF becomes steeper with depth) and lateral slip rate increases with depth (reduced slip partitioning because second-order faults cease at shallower depths, Hergert & Heidbach 2010). Therefore, despite the significant dip-slip rate on the Prince's Islands Segment (Fig. 6) slip is basically in a strike-slip sense.

This apparent contradiction may resolve the problems in interpreting the nature of this fault segment (e.g. Örgülü 2011). The Prince's Islands Segment has been considered as being a pure strike-slip fault which is supported by focal mechanisms and by the fact that the MMF follows approximately a small circle of a Marmara block (Le Pichon *et al.* 2003). The Prince's Islands Segment has been also considered as being a linking normal faulting segment at a step-over of the MMF, forming the rim of a subsiding pull apart basin (Armijo *et al.* 2002). A further possibility is the extinction of pull-apart basins in the past along with a transition to a pure strike-slip fault, which implies that the fault would have become inactive in a dip-slip sense (Rangin *et al.* 2004; Örgülü 2011). Our results indicate that although the fault slips basically in a strike-slip sense there is nevertheless significant (up to 4.5 mm a^{-1}) dip-slip motion. This result concerns not only the interpretation of the structures but it is also important with respect to potential tsunami hazard.

7.2 Character of the fault system

A fault slip pattern as shown in Fig. 7 is expectable from a large-scale negative flower structure. A dominant main fault throughout the crust with predominant strike-slip character agrees with the view of Le Pichon *et al.* (2001, 2003). However, the model also considers subsidiary faults and yields in part considerable lateral and dip-slip rates on these (Figs 3a and 6). This agrees with the view of Armijo *et al.* (2002) that besides the main fault also other faults are involved in accommodating relative plate motion and in shaping the geomorphology.

From earlier test models we found that fault step-overs of the MMF instead of a through-going MMF result in strongly decreased slip rate and in enhanced off-fault deformation. It is also known from other studies that the slip rate along a fault depends on its length and thus on the connectivity between adjoining fault segments (e.g. Bilham & Bodin 1992). In case of a mechanically segmented MMF west-directed motion would be transferred to the northern block, which is not indicated by the results and the GPS observations. We therefore conclude that the MMF is, though not necessarily geometrically but mechanically through-going, at least at depth.

The preferred fault geometry in this study can be described as a through-going main fault with prevailing strike-slip character, which also comprises non-vertical sections exhibiting oblique slip. Near the Tuzla and Ganos Bends the MMF becomes less steep allowing dip-slip at the releasing sides of the bends. The Çınarcık and Tekirdağ Basins can be interpreted as half grabens that tilt towards the dipping MMF. Second-order faults with oblique or dip-slip motion accompany the MMF. An extensional component is taken up by dip-slip, while footwall blocks are stable leading to subsidence and tilting of basement blocks (Laigle *et al.* 2008). Deep-rooted faults are necessary to explain the downthrown basement in the North Marmara Trough that is evident from seismic sections (Laigle *et al.* 2008). Although the modelled vertical motion pattern in agreement with observations is not a definite proof of the appropriateness of the incorporated 3-D fault geometry and fault slip rate, it is nevertheless a strong indication for this.

8 FAULT SLIP RATES AND SEISMIC HAZARD

Fault slip rates are an integral part of seismic hazard assessment. Parsons *et al.* (2000) and Erdik *et al.* (2004) used 22 mm a^{-1} on the MMF to constrain recurrence intervals of characteristic earthquakes and 17–24 mm a^{-1} on the MMF have been used to infer stressing rates for estimates of changes of Coulomb failure stress (ΔCFS) (Hubert-Ferrari *et al.* 2000; Lorenzo-Martin *et al.* 2006; Muller *et al.* 2006; Pondard *et al.* 2007). Kalkan *et al.* (2009) used 20 mm a^{-1} even on the small secondary faults in the Marmara Sea to infer the activity rate of characteristic earthquakes (Kalkan *et al.* 2009). This sums up to 10–123 mm a^{-1} relative displacement along N–S profiles of the Marmara Sea region.

Fault slip rates were also used to estimate the potential coseismic slip on particular segments of the MMF based on the elapsed time since the last major earthquake. Studies using the higher MMF slip rates thus estimated a slip deficit of 4.5–5.5 m (Hubert-Ferrari *et al.* 2000; Pınar *et al.* 2003), whereas our study results in values between 3.1 and 4.3 m. However, this is still equivalent to an $M \sim 7.6$ earthquake if the whole segment ruptured at once or to two smaller events of $M \sim 7.2$ (Hergert & Heidbach 2010).

Furthermore, the inferred characteristics of fault slip rate explain the locations and dimensions of historical earthquakes. The remarkable decrease in fault slip rate between the eastern Izmit Bay and Tuzla Bend of 3–4 mm a^{-1} (Fig. 3a) may have contributed to arrest the 1999 Izmit earthquake in the western Izmit Bay. Based on the modelled fault slip rates we also suggest that historical earthquakes on the Prince's Islands Segment are more frequent than on the fault at the southern margin of the Çınarcık Basin.

The modelled slip rate on the MMF provides a basis for answering the question whether propagating earthquake sequences typical for the NAF (Stein *et al.* 1997) are also characteristic for the Marmara Sea. From the modelled lateral variations in fault slip rate we conclude that the tectonic loading conditions on the faults beneath the Marmara Sea are not as uniform as on the NAF east of the Marmara Sea, where the NAF has a rather simple structure. Therefore, the occurrence of earthquakes is not likely in that remarkable chronological and spatial order in the Marmara Sea—at least not in every seismic cycle. Armijo *et al.* (2002, 2005) and Pondard *et al.* (2007) draw the same conclusion from the complex fault structure in the Marmara Sea with natural barriers like bends or interacting faults which inhibit uniform propagation of earthquakes. In contrast, Le Pichon *et al.* (2003) claim that the slip rate is uniform throughout the whole length of the MMF and consequently they consider a large rupture through the whole Marmara Sea as possible. From our findings as well as from the stress field results presented in the complementary Paper II this seems to be less likely than a segmentation of the seismic gap into two or more ruptures, which would have lower magnitudes, respectively.

9 CONCLUSIONS

We presented a 3-D geomechanical model for the Marmara Sea that fits the contemporary 3-D kinematic observations derived from

Downloaded from https://academic.oup.com/gji/article/185/3/1073/601038 by guest on 12 March 2022

GPS, geological and geomorphological data. From our results we conclude:

(1) The 3-D kinematic results fit the model-independent observations, from timescales which range from interseismic periods (GPS) to several thousand years (fault slip rates from geological and palaeoseismological data and geomorphologic constraints).

(2) Although the MMF accounts for the dominant part of relative Anatolia–Eurasia plate motion (12.8–17.8 mm a^{-1}), relative plate motion in the Marmara Sea region has to be distinguished from the slip rate on the MMF. Second-order faults, dip-slip and internal deformation contribute to the relative plate motion.

(3) The modelled uplift and subsidence rates largely coincide with both, the observed pattern and rates. The present morphology is reflected by the modelled vertical motion, which suggests that tectonic processes have been important in shaping the seafloor. The modelled characteristics of the subsidence in the basins suggest that the implemented fault geometry is reasonable, that is, asymmetric half grabens bounded by a dominating through-going MMF on one side and synthetic normal faults on the other. Vertical motion is to a large extent fault controlled.

(4) As available geodetic constraints may be met by different models of different fault geometries and fault slip distributions it is important to ensure appropriate fault geometries and representation of the kinematics, that is, allowing for internal deformation and dynamically consistent fault slip. Discrepancies between geological and geodetic fault slip rates can be due to this issue.

(5) We find that the post-seismic signal from the 1912 and 1894 earthquakes is negligible in the decade before the 1999 Izmit earthquake.

(6) In contrast to the 3-D fault geometry, material properties have little influence on the kinematics. A dislocation model using the boundary element method would probably result in a similar kinematics. However, for the dynamic model results material properties play a major role (see complementary Paper II).

In the complementary Paper II we will show that the 3-D stress state of this model widely fits also the stress observations in the Marmara Sea. This would imply that our overall goal to construct a model that is consistent with both, kinematic and dynamic observations is attained. The presented model concept can be transferred to other strike-slip regions where complex 3-D fault systems take up relative plate motion.

ACKNOWLEDGMENTS

In particular, we thank A. Hirn for very fruitful discussions on the 3-D kinematics of the Marmara Sea fault system. We also thank K. Fuchs and F. Wenzel for helpful suggestions. We thank the editor Duncan Agnew and two anonymous reviewers for their comments and suggestions. This work was supported by the CEDIM Project at Universität Karlsruhe (TH) and GFZ German Research Centre for Geosciences, by the Heidelberg Academy of Sciences and Humanities and by the Task Force VII 'Temporal and Spatial Changes of Stress and Strain' of the International Lithosphere Program.

REFERENCES

Aksoy, M.E., Meghraoui, M., Ferry, M., Çakir, Z., Akyüz, S., Karabacak, V. & Altunel, E., 2006. Fault characteristics, segmentation and paleoseismology along the 9 August 1912 Ganos earthquake-rupture (North Anatolian Fault, Turkey), *Geophys. Res. Abs.*, **8**, SRef-ID: 1607-7962/gra/EGU1606-10002.

Aksu, A.E., Calon, T.J., Hiscott, R.N. & Yaşar, D., 2000. Anatomy of the North Anatolian Fault Zone in the Marmara Sea, Western Turkey: extensional basins above a continental transform, *GSA Today*, **10**(6), 3–7.

d'Alessio, M.A., Williams, C.F. & Bürgmann, R., 2006. Frictional strength heterogeneity and surface heat flow: implications for the strength of the creeping San Andreas fault. *J. geophys. Res*, **111**(B05410), doi:10.1029/2005JB003780.

Alpar, B. & Yaltırak, C., 2002. Characteristic features of the North Anatolian Fault in the eastern Marmara region and its tectonic evolution, *Mar. Geol.*, **190**, 329–350, PII:S0025-3227(0002)00353-00355

Ambraseys, N., 2002. The seismic activity of the Marmara Sea region over the last 2000 years, *Bull. seism. Soc. Am.*, **92**, 1–18.

Ambraseys, N., 2006. Comparison of frequency of occurrence of earthqaukes with slip rates from long-term seismicity data: the cases of Gulf of Corinth, Sea of Marmara and Dead Sea Fault Zone, *Geophys. J. Int.*, **165**, 516–526.

Armijo, R., Meyer, B., Hubert, A. & Barka, A., 1999. Westward propagation of the North Anatolian fault into the northern Aegean: timing and kinematics, *Geology*, **27**, 267–270.

Armijo, R., Meyer, B., Navarro, S., King, G. & Barka, A., 2002. Asymmetric slip partitioning in the Sea of Marmara pull-apart: a clue to propagation processes of the North Anatolian Fault? *Terra Nova*, **13**, 80–86.

Armijo, R., Flerit, F., King, G. & Meyer, B., 2003. Linear elastic fracture mechanics explains the past and present evolution of the Aegean, *Earth planet. Sci. Lett.*, **217**, 85–95.

Armijo, R., *et al*., 2005. Submarine fault scarps in the Sea of Marmara pull-apart (North Anatolian Fault): implications for seismic hazard in Istambul, *Geochem. Geophys. Geosyst.*, **6**, doi:10.1029/2004GC000896.

Avşar, Ü. & İşseven, T., 2009. Regional clockwise rotation of the Armutlu Penisnula, Western Turkey, resolved from paleomagnetic study of Eocene volcanics, *Tectonophysics*, **475**, 415–422.

Ayhan, M.E., Demir, C., Lenk, O., Kiliçogul, A., Altiner, Y., Barka, A.A., Ergintav, S. & Özener, H., 2002. Interseismic strain accumulation in the Marmara Sea Region, *Bull. seism. Soc. Am.*, **92**, 216–229.

Barka, A., 1997. Neotectonics of the Marmara region. in *Active Tectonics of Northwestern Anatolia: The MARMARA Poly-Project*, pp. 329–374, eds Schindler, C. & Pfister, M., vdf Hochschulverlag AG ETH, Zürich.

Barka, A.A. & Kadinsky-Cade, C., 1988. Strike-slip fault geometry in Turkey and its influence on earthquake activity, *Tectonics*, **7**, 663–684.

Bayrakcı, G., 2009. Hétérogénéité 3D de la croûte supérieure sous la Mer de Marmara: tomographie sur une grille de sismomètres fond de mer et de profils de tirs, *PhD thesis*, Institut de Physique du Globe de Paris.

Bécel, A., *et al*., 2009. Moho, crustal architecture and deep deformation under the North Marmara Trough, from the Seismarmara Leg1 offshore-onshore reflection-refraction survey, *Tectonophysics*, **467**, 1–21.

Bécel, A., Laigle, M., de Voogd, B., Hirn, A., Taymaz, T., Yolsal-Cevikbilen, S. & Shimamura, H., 2010. North Marmara Trough architecture of basin infill, basement and faults, from PSDM reflection and OBS refraction seismics, *Tectonophysics*, **490**, 1–14.

Bilham, R. & Bodin, P, 1992. Fault zone connectivity: slip rates on faults in the San Francisco Bay Area, California, *Science*, **258**, 281–284.

Bird, P., 1998. Testing hypotheses on plate-driving mechanisms with global lithosphere models including topography, thermal structure, and faults, *J. geophys. Res.*, **103**(B5), 10 115–10 129.

Biryol, C.B., *et al*., 2008. NAF experiment: seismic anisotropy beneath Northern Anatolia from shear-wave splitting, *EOS, Trans. Am. geophys. Un.*, **89**(53), Abstract T21A-1916.

Brocher, T.M., 2005. Empirical relations between elastic wavespeeds and density in the Earth's crust, *Bull. seism. Soc. Am.*, **95**, doi:10.1785/0120050077.

Byerlee, J.D., 1978. Friction of rocks, *Pure appl. Geophys.*, **116**, 615–626.

Cai, J. & Grafarend, E.W., 2007. Statistical analysis of geodetic deformation (strain rate) derived from the space geodetic measurements of BIFROST Project in Fennoscandia, *J. Geodyn.*, **43**, 214–238.

Carton, H., *et al*., 2007. Seismic imaging of the three-dimensional architecture of the Çınarcık Basin along the North Anatolian Fault, *J. geophys. Res.*, **112**, doi:10.1029/2006JB004548.

Downloaded from https://academic.oup.com/gji/article/185/3/1073/601038 by guest on 12 March 2022

Cormier, M.-H., *et al*., 2006. North Anatolian Fault in the Gulf of Izmit (Turkey): rapid vertical motion in response to minor bends of a nonvertical continental transform, *J. geophys. Res,* **111**, doi:10.1029/2005JB003633.

Elmas, A., 2003. Late Cenozoic tectonics and stratigraphy of northwestern Anatolia: the effects of the North Anatolian Fault to the region, *Int. J. Earth Sci. (Geol. Rundschau),* **92**, 380–396, doi:10.1007/s00531-003-0322-2.

Elmas, A. & Yiğitbaş, E., 2001. Ophiolite emplacement by strike-slip tectonics between the Pontide Zone and the Sakarya Zone in northwestern Anatolia, Turkey, *Int. J. Earth Sci. (Geol Rundschau),* **90**, 257–269, doi: 10.1007/s005310000129.

Emre, Ö., Erkal, T., Tchepalyga, A., Kazancı, N., Kecer, M. & Ünay, E., 1998. Neogene-Quaternary evolution of the eastern Marmara region, northwest Turkey, *Minerol. Res. Expl. Bull.,* **120**, 119–145.

Emre, Ö., Özaksoy, V. & Çağatay, N. 2006. Guide Book. Field Trip to the North Anatolian Fault System Between Izmit and Yalova, in *International Workshop in Comparative Studies of the North Anatolian Fault and the San Andreas Fault,* 2006 August 14–18, Istanbul.

Erdik, M., Demircioglu, M., Sesetyan, K., Durukal, E. & Siyahi, B., 2004. Earthquake hazard in Marmara Region, Turkey, *Soil Dyn. Earthq. Eng.,* **24**, 605–631.

Ergün, M. & Özel, E., 1995. Structural relationship between the Sea of Marmara Basin and the North Anatolian Fault Zone, *Terra Nova,* **7**, 278–288.

Eyidoğan, H., 1988. Rates of crustal deformation in western Turkey as deduced from major earthquakes, *Tectonophysics,* **148**, 83–92.

Flerit, F., Armijo, R., King, G. & Meyer, B., 2004. The mechanical interaction between the propagating North Anatolian Fault and the back-arc extension in the Aegean, *Earth planet. Sci. Lett.,* **224**, 347–362, doi:10.1016/j.epsl.2004.05.028.

Geist, E.L. & Andrews, D.J., 2000. Slip rates on San Fransico Bay area faults from anelastic deformation of the continental lithosphere. *J. geophys. Res,* **105**, B11, 25543–25552.

Gomez, F., *et al*., 2007. Global Positioning System measurements of strain accumulation and slip transfer through the restraining bend along the Dead Sea fault system in Lebanon, *Gephys. J. Int.,* **168**, 1021–1028.

Hatzfeld, D., *et al*., 2001. Shear wave anisotropy in the upper mantle beneath the Aegean related to internal deformation, *J. geophys. Res.,* **106**, 30737–30753.

Heidbach, O. & Drewes, H., 2003. 3-D finite element model of major tectonic processes in the Eastern Mediterranean, in *New insights in Structural Interpretation and Modelling,* Geol. Soc. Spec. Pub. Vol. 212, pp. 261–274, ed. Nieuwland, D., Geological Society, London, doi.10.1144/GSL.SP.2003.212.01.17.

Hergert, T. & Heidbach, O., 2010. Slip-rate variability and distributed deformation in the Marmara Sea fault system, *Nat. Geosci.,* **3,** 132–135, doi:10.1038/NGEO739.

Hergert, T. & Heidbach, O., 2011. Geomechanical model of the Marmara Sea region—II. 3D contemporary background stress field, *Geophys. J. Int.,* in press, doi:10.1111/j.1365-246X.2011.04992.x. (this issue) (Paper II).

Hubert-Ferrari, A., Barka, A., Jacques, E., Nalbant, S., Meyer, B., Armijo, R., Tapponier, P. & King, G.C.P., 2000. Seismic hazard in the Marmara Sea region following the 17 August 1999 Izmit earthquake, *Nature,* **404**, 269–271.

Hubert-Ferrari, A., Armijo, R., King, G., Mayer, B. & Barka, A., 2002. Morphology, displacement, and slip rates along the North Anatolian Fault, Turkey, *J. geophys. Res,* **107**, B10, 2235, doi:10.1029/2001JB000393.

Hubert-Ferrari, A., King, G., Manighetti, I., Armijo, R., Meyer, B. & Tapponnier, P., 2003. Long-term elasticity in the continental litosphere: modelling the Aden Ridge propagation and the Anatolian extrusion process, *Geophys. J. Int.,* **153**, 111–132.

Jackson, J. & McKenzie, D., 1984. Active tectonics of the Alpine-Himalayan Belt between western Turkey and Pakistan, *Geophys. J. R. astr.,* **77**, 185–264.

Jamison, D.B. & Cook, N.G.W., 1980. Note on measured values for the state of stress in the Earth's crust, *J. geophys. Res,* **85**, 1833–1838.

Jiménez-Munt, I. & Sabadini, R., 2002. The block-like behavior of Anatolia envisaged in the modeled and geodetic strain rates, *Geophys. Res. Lett.,* **29**, 1978, doi:10.1029/2002GL015995.

Jones, C.H. & Wesnousky, S.G., 1992. Variations in strength and slip rate along the San Andreas fault system, *Science,* **256**, 83–86.

Kalkan, E., Gülkan, P., Yılmaz, N. & Çelebi, M., 2009. Reassessment of probabilistic seismic hazard in the Marmara region, *Bull. seism. Soc. Am.,* **99**, 4, 2127–2146, doi:10.1785/0120080285.

Kanbur, Z., Alptekin, Ö., Utkucu, M. & Kanbur, S., 2007. Imaging the basin and fault geometry from the multichannel seismic reflection data in the Tekirdağ Basin, Marmara Sea, Turkey, *Geophys. J. Int,* **169**, 659–666 doi:10.1111/j.1365-1246X.2007.03356.x.

Kiratzi, A., 1993. A study on the active crustal deformation of the North and East Anatolian Fault Zones, *Tectonophysics,* **225**, 191–203.

Kiratzi, A.A. & Papazachos, C.B., 1995. Active crustal deformation from the Azores triple junction to the Middle East, *Tectonophysics,* **243**, 1–24.

Koral, H., 2007. Modes, rates and geomorphological consequences of active tectonics in the Marmara Region, NW Turkey: a critical overview based on seismotectonic field observations, *Quat. Int.,* **167–168**, 149–161, doi:10.1016/j.quaint.2007.02.1023.

Kozacı, Ö., Dolan, J.F., Finkel, R. & Hartleb, R., 2007. Late Holocene slip rate for the North Anatolian fault, Turkey, from cosmogenic 36Cl geochronology: implications for the constancy of fault loading and strain release rates, *Geology,* **35**, 867–870, doi:10.1130/G23187A.23181.

Kozacı, Ö., Dolan, J.F. & Finkel, R.C., 2009. A Late Holocene slip rate for the central North Anatolian fault, at Tahtaköprü, Turkey, from cosmogenic 10Be geochronology: implications for fault loading and strain release rates, *J. geophys. Res.,* **114**, B01405, doi:10.1029/2008JB005760.

Kürçer, A., Chatzipetros, A., Tutkun, S.Z., Pavlides, S., Ate, Ö. & Valkaniotis, S., 2008. The Yenice–Gönen active fault (NW Turkey): active tectonics and palaeoseismology, *Tectonophysics,* **453**, 263–275, doi:10.1016/j.tecto.2007.07.010.

Kurtuluş, C. & Canbay, M.M., 2007. Tracing the middle strand of the North Anatolian Fault Zone through the southern Sea of Marmara based on seismic reflection studies, *Geo-Mar Lett.,* **27**, 27–40, doi:10.1007/s00367-006-0050-2.

Laigle, M., Becél, A., de Voogd, B., Hirn, A., Taymaz, T., Özalaybey, S. & Team, S.L., 2008. A first deep seismic survey in the Sea of Marmara: deep basins and whole crust architecture and evolution, *Earth planet. Sci. Lett.,* **270**, 168–179.

Le Pichon, X., Chamot-Rooke, N., Lallemant, S., Noomen, R. & Veis, G., 1995. Geodetic determination of kinematics of Central Greece with respect to Europe: implications for Eastern Mediterranean, *J. geophys. Res.,* **100**, 12675–12690.

Le Pichon, X., *et al*., 2001. The active main Marmara fault, *Earth planet. Sci. Lett.,* **192**, 595–616.

Le Pichon, X.L., Chamot-Rooke, A., Rangin, C. & Sengör, A.M.C., 2003. The North Anatolian fault in the Sea of Marmara, *J. geophys. Res.,* **108**, doi:10.1029/2002JB001862.

Lorenzo-Martin, F., Roth, F. & Wang, R., 2006. Elastic and inelastic triggering of earthquakes in the North Anatolian Fault zone, *Tectonophysics,* **424**(3–4), 271–289, doi:10.1016/j.tecto.2006.03.046.

Mayer, L. & Lu, Z., 2001. Elastic rebound following the Kocaeli earthquake, Turkey, recorded using synthetic aperture radar interferometry, *Geology,* **29**, 6, 495–498.

McClusky, S., *et al*., 2000. Global Positioning System constraints on plate kinematics and dynamics in the eastern Mediterranean and Caucasus, *J. geophys. Res.,* **105**, 5695–5719.

McHugh, C.M.G., Seeber, L., Cormier, M.-H., Dutton, J., Cagatay, N., Polonia, A., Ryan, W.B.F. & Gorur, N., 2006. Submarine earthquake geology along the North Anatolia Fault in the Marmara Sea, Turkey: a model for transform basin sedimentation, *Earth planet. Sci. Lett.,* **248**, 661–684, doi:10.1016/j.epsl.2006.05.038.

McKenzie, D., 1972. Active tectonics of the Mediterranean region, *Geophys. J. R. astr. Soc.,* **30**, 109–185.

Meade, B.J., Hager, B.H., McClusky, S.C., Reilinger, R., Ergintav, S., Lenk, O., Barka, A. & Özener, H., 2002. Estimates of seismic potential in the Marmara Sea region from block models of secular deformation

Downloaded from https://academic.oup.com/gji/article/185/3/1073/601038 by guest on 12 March 2022

constrained by GPS measurements, *Bull. seism. Soc. Am.*, **92**, 208–215.

Meghraoui, M., *et al*., 2004. Faulting behaviour along the 1912 Ganos Fault segment west of the Marmara Sea: results from paleoseismic investigations, *Geophys. Res. Abstr.*, **6**, SRef-ID:1607-7962/gra/EGU04-A-06211.

Motagh, M., Hoffmann, J., Kampes, B., Baes, M. & Zschau, J., 2007. Strain accumulation across the Gazikoy–Saros segment of the North Anatolian Fault inferred from Persistent Scatterer Interferometry and GPS measurements, *Earth planet. Sci. Lett.*, **255**, 432–444.

Muller, J.R. & Aydin, A., 2005. Using mechanical modeling to constrain fault geometries proposed for the northern Marmara Sea, *J. geophys. Res.*, **110**, doi:10.1029/2004JB003226.

Muller, J.R., Aydin, A. & Wright, T.J., 2006. Using an elastic dislocation model to investigate static Coulomb stress change scenarios for earthquake ruptures in the eastern Marmara Sea region, Turkey, in *Analogue and Numerical Modelling of Crustal-Scale Processes*, Geol. Soc. Spec. Pub. Vol. 253, pp. 397–414, eds. Buiter, S.J.H. & Schreuers, G., Geological Society, London, doi:10.1144/GSL.SP.2006.253.01.21.

Noomen, R., Springer, T.A., Ambrosius, B.A.C., Herzberger, K., Kuijper, D.C., Mets, G.-J., Overgaauw, B. & Wakker, K.F., 1996. Crustal deformations in the mediterranean area computed from SLR and GPS observations, *J. Geodyn.*, **21**(1), 73–96.

Norris, R.J. & Cooper, A.F., 2000. Late quaternary slip rates and slip partitioning on the Alpine Fault, New Zealand, *J. Struct. Geol.*, **23**, 507–520.

Okay, A.I., Demirbağ, E., Kurt, H., Okay, N. & Kuşçu, İ., 1999. An active deep marine strike-slip basin along the North Anatolian fault in Turkey, *Tectonics*, **18**, 129–147.

Okay, N. & Okay, A.I., 2002. Tectonically induced Quaternary drainage diversion in the northeastern Aegean, *J. Geol. Soc. Lond.*, **159**, 393–399.

Oktay, F.Y., Gökaşan, E., Sakınç, M., Yaltırak, C., C., I. & Demirbağ, E., 2002. The effects of the North Anatolian Fault Zone on the latest connection between Black Sea and Sea of Marmara, *Mar. Geol.*, **190**, 367–382.

Oral, M.B., Reilinger, R.E., Toksöz, M.N., King, R.W., Barka, A.A., Kinik, I. & Lenk, O., 1995. Global Positioning System offers evidence of plate motions in the eastern Mediterranean, *EOS, Trans. Am. geophys. Union*, **76**, 9–11.

Örgülü, G., 2011. Seismicity and source parameters for small-scale earthquakes along the splays of the North Anatolian Fault (NAF) in the Marmara Sea, *Geophys. J. Int.*, **184**, 385–404, doi:10.1111/j.1365-246X.2010.04844.x.

Papazachos, B.C. & Kiratzi, A.A., 1996. A detailed study of the active crustal deformation in the Aegean and surrounding area, *Tectonophysics*, **253**, 129–153.

Parke, J.R., White, R.S., McKenzie, D., Minshull, T.A., Bull, J.M., Kuşçu, I., Görür, N. & Şengör, C., 2002. Interaction between faulting and sedimentation in the Sea of Marmara, western Turkey, *J. geophys. Res.*, **107**, doi:10.1029/2001JB000450.

Parsons, T., 2004. Recalculated probability of M7 earthquakes beneath the Sea of Marmara, Turkey, *J. geophys. Res.*, **109**, B05304, doi:10.1029/2003JB002667.

Parsons, T., Toda, S., Stein, R.S., Barka, A. & Dietrich, J.H., 2000. Heightened odds of large earthquakes near Istanbul: an interaction-based probability calculation, *Science*, **288**, 661–664.

Pınar, A., Y. Honkura, M. & Kikuchi, A., 1996. Rupture model for the 1967 Mudurnu Valley, Turkey earthquake and its implication for seismotectonics in the Western Part of the North Anatolian Fault Zone, *Geophys. Res. Lett.*, **23**, 29–32.

Pınar, A., Kuge, K. & Honkura, Y., 2003. Moment tensor inversion of recent small to moderate sized earthquakes: implications for seismic hazard and active tectonics beneath the Sea of Marmara, *Geophys. J. Int.*, **153**, 133–145.

Polonia, A., *et al*., 2004. Holocene slip rate of the North Anatolian Fault beneath the Sea of Marmara, *Earth planet. Sci. Lett.*, **227**, 411–426.

Pondard, N., Armijo, R., King, G.C.P., Meyer, B. & Flerit, F., 2007. Fault interactions in the Sea of Marmara pull. apart (North Anatolian Fault): earthquake clustering and propagating earthquake sequences, *Geophys. J. Int.*, **171**(3), 1185–1197, doi:10.1111/j.1365-1246X.2007.03580.x.

Provost, A.-S., Chéry, J. & Hassani, R., 2003. 3D mechanical modeling of the GPS velocity field along the North Anatolian fault, *Earth planet. Sci. Lett.*, **209**, 361–377 doi:310.1016/S0012-1821X(1003)00099-00092.

Rangin, C., Pichon, X.L., Demirbag, E. & Imren, C., 2004. Strain localization in the Sea of Marmara: Propagation of the North Anatolian Fault in a now inactive pull-apart, *Tectonics*, **23**, doi:10.1029/2002TC001437.

Reasenberg, P.A., & Simpson, R.W., 1992. Response of regional seismicity to the static stress change produced by the Loma Prieta earthquake, *Science*, **255**, 1687–1690.

Reilinger, R.E., *et al*., 2000. Coseismic and postseismic fault slip for the 17 August 1999, M = 7.5, Izmit, Turkey earthquake, *Science*, **289**, 1519, doi:10.1126/science.289.5484.1519.

Reilinger, R., *et al*., 2006. GPS constraints on continental deformation in the Africa-Arabia-Eurasia continental collision zone and implications for the dynamics of plate interaction, *J. geophys. Res.*, **111**, doi:10.1029/2005JB004051.

Rockwell, T., Barka, A., Dawson, T., Akyuz, S. & Thorup, K., 2001. Paleoseismology of the Gazikoy-Saros segement of the North Anatolia fault, northwestern Turkey: comparison of the historical and paleoseismic records, implications of regional seismic hazard, and models of earthquake recurrence, *J. Seismol.*, **5**, 433–448.

Rockwell, T.K., *et al*. 2006. Paleoseismology of the 1912, 1944 and 1999 ruptures on the North Anatolian fault: implications for late Holocene patterns of strain release, in *International Workshop in Comparative Studies of the North Anatolian Fault and the San Andreas Fault*, pp. 11–12, 2006 August 14–18, Istanbul.

Rockwell, T., *et al*., 2009. Paleoseismology of the North Anatolian Fault near the Marmara Sea: implications for fault segmentation and seismic hazard, in *Paleoseismology: Historical and Prehistorical Records of Earthquake Ground Effects for Seismic Hazard Assessment*, Geol. Soc. Spec. Pub. Vol. 316, pp. 31–54, eds Reicherter, K., Michetti, A.M. & Silva, P.G., Geological Society, London, doi:10.1144/SP316.3.

Schindler, C., 1997. Geology of northwestern Turkey: Results of the MARMARA Poly-Project, in *Active Tectonics of Northwestern Anatolia-The MARMARA Poly-Project*, pp. 329–374, eds Schindler, C. & Pfister, M., vdf Hochschulverlag AG ETH, Zürich.

Seeber, L., Embre, O., Cormier, M.-H., Sorlien, C.C., McHugh, C.M.G., Polonia, A., Ozer, N. & Cagatay, N., 2004. Uplift and subsidence from oblique slip: the Ganos-Marmara bend of the North Anatolian Transform, Western Turkey, *Tectonophysics*, **391**, 239–258, doi:10.1016/j.tecto.2004.07.015.

Seeber, L., Cormier, M.-H., McHugh, C., Emre, O., Polonia, A. & Sorlien, C., 2006. Rapid subsidence and sedimentation from oblique slip near a bend on the North Anatolian transform fault in the Marmara Sea, Turkey, *Geology*, **34**, 933–936.

Şengör, A.M.C., Tüysüz, O., Sakınç, M., Eyidoğan, H., Görür, N., Pichon, X.L. & Rangin, C., 2005. The North Anatolian fault: a new look, *Ann. Rev. Earth planet. Sci.*, **33**, 37–112, doi:10.1146/annurev.earth.32.101802.120415.

Stein, R.S., Barka, A.A. & Dietrich, J.H., 1997. Progressive failure on the North Anatolian fault since 1939 by earthquake stress triggering, *Geophys. J. Int.*, **128**, 594–604.

Straub, C., Kahle, H.G. & Schindler, C., 1997. GPS and geologic estimates of the tectonic activity in the Marmara Sea region, NW Anatolia, *J. geophys. Res.*, **102**, 27,587–527,601.

Townend, J. & Zoback, M.D., 2004. Regional Tectonic stress near the San Andreas fault in central and Southern California, *Geophys. Res. Lett.*, **31**, doi:10.1029/2003GL018918.

Vernant, P. & Chéry, J., 2006. Low fault friction in Iran implies localized deformation for the Arabia–Eurasia collision zone, *Earth planet. Sci. Lett.*, **246**, 197–206 doi:10.1016/j.epsl.2006.04.021.

Walter, T.R., *et al*., 2010. Satellite Monitoring of Hazards: a focus on Istanbul, Turkey, *EOS, Trans., Am. geophys. Un.*, **91**, 36.

Downloaded from https://academic.oup.com/gji/article/185/3/1073/601038 by guest on 12 March 2022

Westaway, R., 1994. Present-day kinematics of the Middle East and eastern Mediterranean, *J. geophys. Res.*, **99**, 12 071–12 090.

Yaltırak, C. & Alpar, B. 2002a. Kinematics and evolution of the northern branch of the North Anatolian Fault (Ganos Fault) between the Sea of Marmara and the Gulf of Saros, *Mar. Geol.*, **190**, 351–366.

Yaltırak, C. & Alpar, B. 2002b. Evolution of the middle strand of the North Anatolian Fault and shallow seismic investigation of the southeastern Marmara Sea (Gemlik Bay), *Mar. Geol.*, **190**, 307–327.

Yaltırak, C., Sakinc, M., Aksu, A.E., Hiscott, R.N., Galleb, B. & Ulgen, U.B., 2002. Late Pleistocene uplift history along the southwestern Marmara Sea determined from raised coastal deposits and global sea-level variations, *Mar. Geol.*, **190**, 283–305, PII:S0025-3227(02)00351-1.

Zienkiewicz, O.C. & Tayler, R.L., 1994. *The Finite Element Method, Volume 1: Basic Formulations and Linear Problems*, 4th edn, McGraw Hill, London.

Zoback, M.D., *et al*., 1987. New evidence of the state of stress of the San Andreas fault system, *Science*, **238**, 1105–1111.

SUPPORTING INFORMATION

Supporting Information may be found in the online version of this article.

The following figures are included in the file named gji_4991_sm_supplement.pdf:

Figure S1. Moho map.

Figure S2. MAT_grad rock property distribution.

Figure S3. Interseismic velocities and postseismic effects.

Figure S4. Slip rates from previous models.

The geometry of the model along with a readme file is contained in 'geometry.zip'.

Please note: Wiley-Blackwell are not responsible for the content or functionality of any supporting materials supplied by the authors. Any queries (other than missing material) should be directed to the corresponding author for the article.

Downloaded from https://academic.oup.com/gji/article/185/3/1073/601038 by guest on 12 March 2022